Systematic studies of the centrality and $\sqrt{s_{NN}}$ dependence of the $dE_T/d\eta$ and $dN_{\rm ch}/d\eta$ in heavy ion collisions at midrapidity

S. S. Adler,[5] S. Afanasiev,[17] C. Aidala,[5] N. N. Ajitanand,[43] Y. Akiba,[20,38] J. Alexander,[43] R. Amirikas,[12] L. Aphecetche,[45] S. H. Aronson,[5] R. Averbeck,[44] T. C. Awes,[35] R. Azmoun,[44] V. Babintsev,[15] A. Baldisseri,[10] K. N. Barish,[6] P. D. Barnes,[27] B. Bassalleck,[33] S. Bathe,[30] S. Batsouli,[9] V. Baublis,[37] A. Bazilevsky,[39,15] S. Belikov,[16,15] Y. Berdnikov,[40] S. Bhagavatula,[16] J. G. Boissevain,[27] H. Borel,[10] S. Borenstein,[25] M. L. Brooks,[27] D. S. Brown,[34] N. Bruner,[33] D. Bucher,[30] H. Buesching,[30] V. Bumazhnov,[15] G. Bunce,[5,39] J. M. Burward-Hoy,[26,44] S. Butsyk,[44] X. Camard,[45] J.-S. Chai,[18] P. Chand,[4] W. C. Chang,[2] S. Chernichenko,[15] C. Y. Chi,[9] J. Chiba,[20] M. Chiu,[9] I. J. Choi,[52] J. Choi,[19] R. K. Choudhury,[4] T. Chujo,[5] V. Cianciolo,[35] Y. Cobigo,[10] B. A. Cole,[9] P. Constantin,[16] D. G. d'Enterria,[45] G. David,[5] H. Delagrange,[45] A. Denisov,[15] A. Deshpande,[39] E. J. Desmond,[5] O. Dietzsch,[41] O. Drapier,[25] A. Drees,[44] R. du Rietz,[29] A. Durum,[15] D. Dutta,[4] Y. V. Efremenko,[35] K. El Chenawi,[49] A. Enokizono,[14] H. En'yo,[38,39] S. Esumi,[48] L. Ewell,[5] D. E. Fields,[33,39] F. Fleuret,[25] S. L. Fokin,[23] B. D. Fox,[39] Z. Fraenkel,[51] J. E. Frantz,[9] A. Franz,[5] A. D. Frawley,[12] S.-Y. Fung,[6] S. Garpman,[29,*] T. K. Ghosh,[49] A. Glenn,[46] G. Gogiberidze,[46] M. Gonin,[25] J. Gosset,[10] Y. Goto,[39] R. Granier de Cassagnac,[25] N. Grau,[16] S. V. Greene,[49] M. Grosse Perdekamp,[39] W. Guryn,[5] H.-Å. Gustafsson,[29] T. Hachiya,[14] J. S. Haggerty,[5] H. Hamagaki,[8] A. G. Hansen,[27] E. P. Hartouni,[26] M. Harvey,[5] R. Hayano,[8] X. He,[13] M. Heffner,[26] T. K. Hemmick,[44] J. M. Heuser,[44] M. Hibino,[50] J. C. Hill,[16] W. Holzmann,[43] K. Homma,[14] B. Hong,[22] A. Hoover,[34] T. Ichihara,[38,39] V. V. Ikonnikov,[23] K. Imai,[24,38] D. Isenhower,[1] M. Ishihara,[38] M. Issah,[43] A. Isupov,[17] B. V. Jacak,[44] W. Y. Jang,[22] Y. Jeong,[19] J. Jia,[44] O. Jinnouchi,[38] B. M. Johnson,[5] S. C. Johnson,[26] K. S. Joo,[31] D. Jouan,[36] S. Kametani,[8,50] N. Kamihara,[47,38] J. H. Kang,[52] S. S. Kapoor,[4] K. Katou,[50] S. Kelly,[9] B. Khachaturov,[51] A. Khanzadeev,[37] J. Kikuchi,[50] D. H. Kim,[31] D. J. Kim,[52] D. W. Kim,[19] E. Kim,[42] G.-B. Kim,[25] H. J. Kim,[52] E. Kistenev,[5] A. Kiyomichi,[48] K. Kiyoyama,[32] C. Klein-Boesing,[30] H. Kobayashi,[38,39] L. Kochenda,[37] V. Kochetkov,[15] D. Koehler,[33] T. Kohama,[14] M. Kopytine,[44] D. Kotchetkov,[6] A. Kozlov,[51] P. J. Kroon,[5] C. H. Kuberg,[1,27] K. Kurita,[39] Y. Kuroki,[48] M. J. Kweon,[22] Y. Kwon,[52] G. S. Kyle,[34] R. Lacey,[43] V. Ladygin,[17] J. G. Lajoie,[16] A. Lebedev,[16,23] S. Leckey,[44] D. M. Lee,[27] S. Lee,[19] M. J. Leitch,[27] X. H. Li,[6] H. Lim,[42] A. Litvinenko,[17] M. X. Liu,[27] Y. Liu,[36] C. F. Maguire,[49] Y. I. Makdisi,[5] A. Malakhov,[17] V. I. Manko,[23] Y. Mao,[7,38] G. Martinez,[45] M. D. Marx,[44] H. Masui,[48] F. Matathias,[44] T. Matsumoto,[8,50] P. L. McGaughey,[27] E. Melnikov,[15] M. Mendenhall,[49] F. Messer,[44] Y. Miake,[48] J. Milan,[43] T. E. Miller,[49] A. Milov,[44,51] S. Mioduszewski,[5] R. E. Mischke,[27] G. C. Mishra,[13] J. T. Mitchell,[5] A. K. Mohanty,[4] D. P. Morrison,[5] J. M. Moss,[27] F. Mühlbacher,[44] D. Mukhopadhyay,[51] M. Muniruzzaman,[6] J. Murata,[38,39] S. Nagamiya,[20] J. L. Nagle,[9] T. Nakamura,[14] B. K. Nandi,[6] M. Nara,[48] J. Newby,[46] P. Nilsson,[29] A. S. Nyanin,[23] J. Nystrand,[29] E. O'Brien,[5] C. A. Ogilvie,[16] H. Ohnishi,[5,38] I. D. Ojha,[49,3] K. Okada,[38] M. Ono,[48] V. Onuchin,[15] A. Oskarsson,[29] I. Otterlund,[29] K. Oyama,[8] K. Ozawa,[8] D. Pal,[51] A. P. T. Palounek,[27] V. S. Pantuev,[44] V. Papavassiliou,[34] J. Park,[42] A. Parmar,[33] S. F. Pate,[34] T. Peitzmann,[30] J.-C. Peng,[27] V. Peresedov,[17] C. Pinkenburg,[5] R. P. Pisani,[5] F. Plasil,[35] M. L. Purschke,[5] A. K. Purwar,[44] J. Rak,[16] I. Ravinovich,[51] K. F. Read,[35,46] M. Reuter,[44] K. Reygers,[30] V. Riabov,[37,40] Y. Riabov,[37] G. Roche,[28] A. Romana,[25] M. Rosati,[16] P. Rosnet,[28] S. S. Ryu,[52] M. E. Sadler,[1] N. Saito,[38,39] T. Sakaguchi,[8,50] M. Sakai,[32] S. Sakai,[48] V. Samsonov,[37] L. Sanfratello,[33] R. Santo,[30] H. D. Sato,[24,38] S. Sato,[5,48] S. Sawada,[20] Y. Schutz,[45] V. Semenov,[15] R. Seto,[6] M. R. Shaw,[1,27] T. K. Shea,[5] T.-A. Shibata,[47,38] K. Shigaki,[14,20] T. Shiina,[27] C. L. Silva,[41] D. Silvermyr,[27,29] K. S. Sim,[22] C. P. Singh,[3] V. Singh,[3] M. Sivertz,[5] A. Soldatov,[15] R. A. Soltz,[26] W. E. Sondheim,[27] S. P. Sorensen,[46] I. V. Sourikova,[5] F. Staley,[10] P. W. Stankus,[35] E. Stenlund,[29] M. Stepanov,[34] A. Ster,[21] S. P. Stoll,[5] T. Sugitate,[14] J. P. Sullivan,[27] E. M. Takagui,[41] A. Taketani,[38,39] M. Tamai,[50] K. H. Tanaka,[20] Y. Tanaka,[32] K. Tanida,[38] M. J. Tannenbaum,[5] P. Tarján,[11] J. D. Tepe,[1,27] T. L. Thomas,[33] J. Tojo,[24,38] H. Torii,[24,38] R. S. Towell,[1] I. Tserruya,[51] H. Tsuruoka,[48] S. K. Tuli,[3] H. Tydesjö,[29] N. Tyurin,[15] H. W. van Hecke,[27] J. Velkovska,[5,44] M. Velkovsky,[44] L. Villatte,[46] A. A. Vinogradov,[23] M. A. Volkov,[23] E. Vznuzdaev,[37] X. R. Wang,[13] Y. Watanabe,[38,39] S. N. White,[5] F. K. Wohn,[16] C. L. Woody,[5] W. Xie,[6] Y. Yang,[7] A. Yanovich,[15] S. Yokkaichi,[38,39] G. R. Young,[35] I. E. Yushmanov,[23] W. A. Zajc,[9,†] C. Zhang,[9] S. Zhou,[7] S. J. Zhou,[51] and L. Zolin[17]
(PHENIX Collaboration)

[1]*Abilene Christian University, Abilene, Texas 79699, USA*
[2]*Institute of Physics, Academia Sinica, Taipei 11529, Taiwan*
[3]*Department of Physics, Banaras Hindu University, Varanasi 221005, India*
[4]*Bhabha Atomic Research Centre, Bombay 400 085, India*
[5]*Brookhaven National Laboratory, Upton, New York 11973-5000, USA*
[6]*University of California–Riverside, Riverside, California 92521, USA*
[7]*China Institute of Atomic Energy (CIAE), Beijing, People's Republic of China*
[8]*Center for Nuclear Study, Graduate School of Science, University of Tokyo, 7-3-1 Hongo, Bunkyo, Tokyo 113-0033, Japan*
[9]*Columbia University, New York, New York 10027 and Nevis Laboratories, Irvington, New York 10533, USA*
[10]*Dapnia, Commissariat à l'Energie Atomique Saclay, F-91191 Gif-sur-Yvette, France*
[11]*Debrecen University, H-4010 Debrecen, Egyetem tér 1, Hungary*
[12]*Florida State University, Tallahassee, Florida 32306, USA*
[13]*Georgia State University, Atlanta, Georgia 30303, USA*
[14]*Hiroshima University, Kagamiyama, Higashi-Hiroshima 739-8526, Japan*

0556-2813/2005/71(3)/034908(25)/$23.00

[15]*Institute for High Energy Physics (IHEP), Protvino, Russia*
[16]*Iowa State University, Ames, Iowa 50011, USA*
[17]*Joint Institute for Nuclear Research, 141980 Dubna, Moscow Region, Russia*
[18]*KAERI, Cyclotron Application Laboratory, Seoul, Korea*
[19]*Kangnung National University, Kangnung 210-702, Korea*
[20]*KEK, High Energy Accelerator Research Organization, Tsukuba-shi, Ibaraki-ken 305-0801, Japan*
[21]*Central Energy Research Establishment, Research Institute for Particle and Nuclear Physics (RMKI), P.O. Box 49, H-1525 Budapest 114, Hungary*
[22]*Korea University, Seoul 136-701, Korea*
[23]*Russian Research Center "Kurchatov Institute," Moscow, Russia*
[24]*Kyoto University, Kyoto 606, Japan*
[25]*Laboratoire Leprince-Ringuet, Ecole Polytechnique, Centre National de la Recherche Scientifique IN2P3, Route de Saclay, F-91128 Palaiseau, France*
[26]*Lawrence Livermore National Laboratory, Livermore, California 94550, USA*
[27]*Los Alamos National Laboratory, Los Alamos, New Mexico 87545, USA*
[28]*LPC, Université Blaise Pascal, Centre National de la Recherche Scientifique-IN2P3, Clermont-Fd, F-63177 Aubiere Cedex, France*
[29]*Department of Physics, Lund University, Box 118, SE-221 00 Lund, Sweden*
[30]*Institut für Kernphysik, University of Muenster, D-48149 Muenster, Germany*
[31]*Myongji University, Yongin, Kyonggido 449-728, Korea*
[32]*Nagasaki Institute of Applied Science, Nagasaki-shi, Nagasaki 851-0193, Japan*
[33]*University of New Mexico, Albuquerque, New Mexico 87131, USA*
[34]*New Mexico State University, Las Cruces, New Mexico 88003, USA*
[35]*Oak Ridge National Laboratory, Oak Ridge, Tennessee 37831, USA*
[36]*IPN-Orsay, Universite Paris Sud, Centre National de la Recherche Scientifique-IN2P3, BP1, F-91406 Orsay, France*
[37]*Petersburg Nuclear Physics Institute (PNPI), Gatchina, Russia*
[38]*Institute of Physical and Chemical Research (RIKEN), Wako, Saitama 351-0198, Japan*
[39]*RIKEN BNL Research Center, Brookhaven National Laboratory, Upton, New York 11973-5000, USA*
[40]*St. Petersburg State Technical University, St. Petersburg, Russia*
[41]*Universidade de São Paulo, Instituto de Física, Caixa Postal 66318, São Paulo CEP05315-970, Brazil*
[42]*System Electronics Laboratory, Seoul National University, Seoul, Korea*
[43]*Chemistry Department, SUNY at Stony Brook, Stony Brook, New York 11794-3400, USA*
[44]*Department of Physics and Astronomy, SUNY at Stony Brook, Stony Brook, New York 11794, USA*
[45]*SUBATECH, Ecole des Mines de Nantes, Centre National de la Recherche Scientifique-IN2P3, Université de Nantes, BP 20722-44307, Nantes, France*
[46]*University of Tennessee, Knoxville, Tennessee 37996, USA*
[47]*Department of Physics, Tokyo Institute of Technology, Tokyo 152-8551, Japan*
[48]*Institute of Physics, University of Tsukuba, Tsukuba, Ibaraki 305, Japan*
[49]*Vanderbilt University, Nashville, Tennessee 37235, USA*
[50]*Waseda University, Advanced Research Institute for Science and Engineering, 17 Kikui-cho, Shinjuku-ku, Tokyo 162-0044, Japan*
[51]*Weizmann Institute, Rehovot 76100, Israel*
[52]*Yonsei University, IPAP, Seoul 120-749, Korea*

(Received 20 September 2004; published 25 March 2005; corrected 6 April 2005)

The PHENIX experiment at the relativistic heavy ion collider (RHIC) has measured transverse energy and charged particle multiplicity at midrapidity in Au + Au collisions at center-of-mass energies $\sqrt{s_{NN}} = 19.6$, 130, and 200 GeV as a function of centrality. The presented results are compared to measurements from other RHIC experiments and experiments at lower energies. The $\sqrt{s_{NN}}$ dependence of $dE_T/d\eta$ and $dN_{\rm ch}/d\eta$ per pair of participants is consistent with logarithmic scaling for the most central events. The centrality dependence of $dE_T/d\eta$ and $dN_{\rm ch}/d\eta$ is similar at all measured incident energies. At RHIC energies, the ratio of transverse energy per charged particle was found to be independent of centrality and growing slowly with $\sqrt{s_{NN}}$. A survey of comparisons between the data and available theoretical models is also presented.

DOI: 10.1103/PhysRevC.71.034908 PACS number(s): 25.75.Dw

*Deceased.
†PHENIX Spokesperson: zajc@nevis.columbia.edu.

I. INTRODUCTION

The PHENIX experiment at the relativistic heavy ion collider (RHIC) at Brookhaven National Laboratory was designed to measure the properties of matter at extremely high temperatures and densities. Under such conditions, the possibility exists of producing states of matter that have not been observed and studied in the laboratory. Perhaps the best known of these is the quark-gluon plasma (QGP), a matter in which the quarks are not confined within individual baryons but exist as some form of plasma of individual quarks and gluons. It should be emphasized that the exact properties of this matter are not known and that the characterization of the deconfined state, if such a state is produced, will form an essential part of the RHIC program.

One fundamental element of the study of ultrarelativistic collisions is the characterization of the interaction in terms of variables such as the energy produced transverse to the beam direction or the number of charged particles. These variables are closely related to the collision geometry and are important in understanding global properties of the system during the collision.

This paper describes the PHENIX experiment's systematic study of $dE_T/d\eta$ and $dN_{\rm ch}/d\eta$ at midrapidity at center-of-mass energies $\sqrt{s_{NN}} = 19.6$, 130, and 200 GeV. The centrality dependence of $dE_T/d\eta$ and $dN_{\rm ch}/d\eta$ is characterized by the number of participants, determined with a Glauber model, and is studied as a function of the incident energy. $dE_T/d\eta$ and $dN_{\rm ch}/d\eta$ results for all four RHIC experiments are included in this study. The data taken at 19.6 GeV are particularly interesting because they can be compared with data taken at lower energies by the CERN super proton synchroton (SPS) program. Comparisons are also made with results of previous experiments conducted at the Brookhaven alternating-gradient synchroton (AGS) and the CERN SPS for c.m. energies of 4.8, 8.7, and 17.2 GeV. Finally, an extensive set of collision models describing the E_T and $N_{\rm ch}$ distributions are compared with existing data. Appendix A describes the recalculation of non-PHENIX data to make comparison possible. Appendix B contains the PHENIX measurement data.

II. PHENIX DETECTOR

PHENIX is one of four experiments located at RHIC [1]. The PHENIX detector consists of two central spectrometer arms, designated east and west for their location relative to the interaction region, and two muon spectrometers, similarly called north and south. Each central spectrometer arm covers a rapidity range of $|\eta| < 0.35$ and subtends 90° in azimuth. The muon spectrometers both have full azimuthal coverage with a rapidity range of $-2.2 < \eta < -1.2$ (south) and $1.2 < \eta < 2.4$ (north). Additional global detectors are used as input to the trigger and for global event characterization such as vertex, time of event, and centrality determination. A detailed description of the PHENIX detector can be found in [2]. The PHENIX detector subsystems relevant to the physics analysis presented in this paper are listed below.

Charged particle multiplicity was measured with two multiwire proportional chamber (MWPC) layers of the pad chambers (PCs) [3] called PC1 and PC3. These are located in both central arms at the radii of 2.5 and 5.0 m from the beam axis. The PCs cover the full central arm acceptance and have an efficiency greater than 99.5% for minimum ionizing particles. The position resolution of PC1 was measured to be 1.7 by 3 mm; it was twice that for PC3. PC1 and PC3 can distinguish between two particle tracks if they strike the detector with a separation greater than 4 and 8 cm, respectively.

For the transverse energy measurements, a PbSc sampling calorimeter (EMCal) [4] from the PHENIX central spectrometers was used. The front face of EMCal is located 5.1 m from the beam axis. Scintillation light produced in the PbSc EMCal towers is read out through wavelength shifting fibers that penetrate the module. The depth of the PbSc calorimeter is 18 radiation lengths (X_0) which corresponds to 0.85 nuclear interaction lengths. The PbSc calorimeter has an energy resolution of $8.1\%/\sqrt{E\,(\mathrm{GeV})}\oplus 2.1\%$ for test beam electrons, with a measured response proportional to the incident electron energy that is within $\pm 2\%$ over the range $0.3 \leqslant E_e \leqslant 40.0$ GeV [4].

Two identical beam-beam counters (BBCs) [5] each consisting of 64 individual Cherenkov counters with 3-cm quartz glass radiators cover the full azimuthal angle in the pseudorapidity range $3.0 < |\eta| < 3.9$. These detectors provide a minimum biased (MB) event trigger and timing and are also used for event vertex determination. The vertex position resolution for central Au + Au events was 6 mm along the beam axis.

The zero degree calorimeters (ZDCs) [6] are hadronic calorimeters located on both sides of the PHENIX detector. They cover a rapidity region of $|\eta| > 6$ and measure the energy of the spectator neutrons with approximately 20% energy resolution. The BBC and ZDC were used for the centrality determination.

III. DATA ANALYSIS

The analysis procedures for the $dE_T/d\eta$ and $dN_{\rm ch}/d\eta$ measured at $\sqrt{s_{NN}} = 130$ GeV are described in [7] and [8], respectively. In this paper the analysis was improved in the following ways:

- Inflow and outflow corrections were done based on the identified particle data, as opposed to HIJING.
- Corrected trigger efficiency was $92.2^{+2.5}_{-3.0}\%$ instead of $92.0 \pm 2 \pm 1\%$.
- Definition of E_T was modified as discussed below.

The results presented here for $\sqrt{s_{NN}} = 130$ GeV are consistent with results previously published.

The same data samples with zero magnetic field were used for both E_T and $N_{\rm ch}$ measurements at each beam energy. The analyzed numbers of events are approximately 40×10^3, 160×10^3, and 270×10^3 for $\sqrt{s_{NN}} = 19.6$, 130, and 200 GeV, respectively.

The main steps of the analysis procedure are discussed below in connection with the systematic errors associated with them. Some additional details can be found in [9–12].

A. E_T analysis

The transverse energy E_T is defined as

$$E_T = \sum_i E_i \sin\theta_i, \tag{1}$$

where θ_i is the polar angle. The sum is taken over all particles emitted into a fixed solid angle in an event. By convention, E_i is taken to be $E_i^{\rm tot} - m_N$ for baryons, $E_i^{\rm tot} + m_N$ for antibaryons, and $E_i^{\rm tot}$ for all other particles, where $E_i^{\rm tot}$ is the total energy of the particle and m_N is the nucleon mass.[1]

The E_T measurement presented in this paper was performed using the PHENIX PbSc EMCal. The EMCal absolute energy scale was set using the π^0 mass peak reconstructed from pairs of EMCal clusters. The value was checked against a measurement of the minimum ionizing peak for charged particles penetrating along the tower axis and the energy/momentum (E/p) peak of identified electrons and positrons. The uncertainty in the absolute energy scale is 3% in the $\sqrt{s_{NN}} =$ 19.6-GeV data and 1.5% in the 130- and 200-GeV data.

The EMCal acts as a thin but effective hadronic calorimeter at midrapidity at a collider [7]. The mean hadron momenta in the EMCal acceptance are approximately 0.4, 0.55, and 0.9 GeV/c for pion, kaons, and (anti)protons, respectively [13]. Most hadrons stop in the EMCal, depositing all their kinetic energy (at p_T less than 0.35 GeV/c for pions, 0.64 for kaons, and 0.94 for protons).

The average EMCal response to the different particle species was obtained with a GEANT-based [14] Monte Carlo (MC) simulation of the PHENIX detector using the HIJING [15] event generator. The HIJING particle composition and p_T spectra were tuned to the identified charged particle spectra and yields in Au + Au collisions measured by PHENIX [13,16] at $\sqrt{s_{NN}} = 200$ and 130 GeV. The NA49 results [17–19] were used for EMCal response studies for 19.6-GeV data. The "deposited" $E_{T_{\rm EMC}}$ was about 75% of the total E_T "striking" the EMCal. This value varied in the ±1.5% range for different centralities and beam energies.

The uncertainty in the EMCal response to hadrons gave a 3% error to the total E_T. This uncertainty was estimated using a comparison between the simulated energy deposited by hadrons with different momenta and from the test beam data [4]. An additional error of 1.3% at $\sqrt{s_{NN}} = 19.6$ and 200 GeV and 1% at 130 GeV comes from the systematic uncertainties in the particle composition and momentum distribution.

E_T was computed for each event [Eq. (1)] using clusters with energy greater than 30 MeV composed of adjacent towers with deposited energy of more than 10 MeV.[2] The energy losses at the EMCal edges and those due to energy thresholds, 6% each, were estimated with the absolute uncertainty 1.5%.

The first main issue for the E_T measurement is the correction for losses for particles originating within the aperture but whose decay products miss the EMCal (∼10%). The second issue is the inflow contribution (∼24%), which is principally of two types: (1) albedo from the magnet poles and (2) particles originating outside the aperture of the calorimeter but whose decay products hit the calorimeter. The inflow component was checked by comparing the MC simulation and the measurements for events with a vertex just at and inside a pole face of the axial central-spectrometer magnet, for which the calorimeter aperture was partly shadowed. The estimated contribution of the inflow uncertainty to the E_T uncertainty is 3% [7].

Since E_T measurements are based on the sum of all cluster energies in the EMCal, random noise even in a small portion of the total number of EMCal towers (∼15,000 in PbSc) may affect the total energy in the EMCal, particularly in peripheral collisions. This effect was estimated by measuring the total energy in the EMCal in very peripheral events with the collision vertex inside the magnet poles. In this case, the EMCal is fully shadowed and no energy deposit from beam collisions is expected. The estimated contribution was consistent with zero. The uncertainty from this effect contributes 3.5% systematic error to the E_T measurement in the most peripheral bin of 45–50% at $\sqrt{s_{NN}} = 19.6$ GeV, 10% to the most peripheral bin of 65–70% at 130 GeV, and 6% to the bin of 65–70% at 200 GeV. The contribution to the systematic error for central events is negligible.

B. $N_{\rm ch}$ analysis

In the absence of a magnetic field, the particle tracks are straight lines. The number of tracks in the event was determined by combining all hits in PC3 with all hits in PC1. The resulting straight lines were projected onto a plane containing the beam line and perpendicular to the symmetry axis of the PCs. All tracks intersecting the plane at a radius less than 25 cm from the event vertex were accepted. 95±1% of all real tracks in the event pointed back within this radius. The complete set of tracks thus formed contained both real tracks and tracks from a combinatorial background. The latter were determined using a mixed event technique in which each sector in PC1 was exchanged with its neighbor and the resulting combinatorial background measured. The average combinatorial background from the mixed event analysis was subtracted from the data obtained from the real events. Several corrections were subsequently applied.

A correction of 15.3% accounted for nonsensitive mechanical gaps between the PC sectors, inactive electronic readout cards, and dead pads in the PC1 and PC3 detectors. The data were also corrected for the PC efficiency for an isolated hit, measured to be 99.5% using cosmic rays [3]. The combined systematic error from these corrections was estimated to be 2.5% for a single east arm and 2.3% for both east and west arms.

Track losses from the finite double hit resolution of the PCs depend on the event multiplicity. Losses can occur in both the direct counting of tracks and in the combinatorial background subtraction. These two effects were studied in great detail using

[1]The definition of E_i in our earlier publication [7] is different for the antibaryon contribution: $E_i^{\rm tot}$ was used instead of $E_i^{\rm tot} + m_N$. The current definition increases the value of E_T by about 4%, independent of centrality.

[2]In [7] thresholds of 20 and 3 MeV were applied for the cluster and for the tower, respectively. Energy losses due to thresholds were properly accounted for in both analyses.

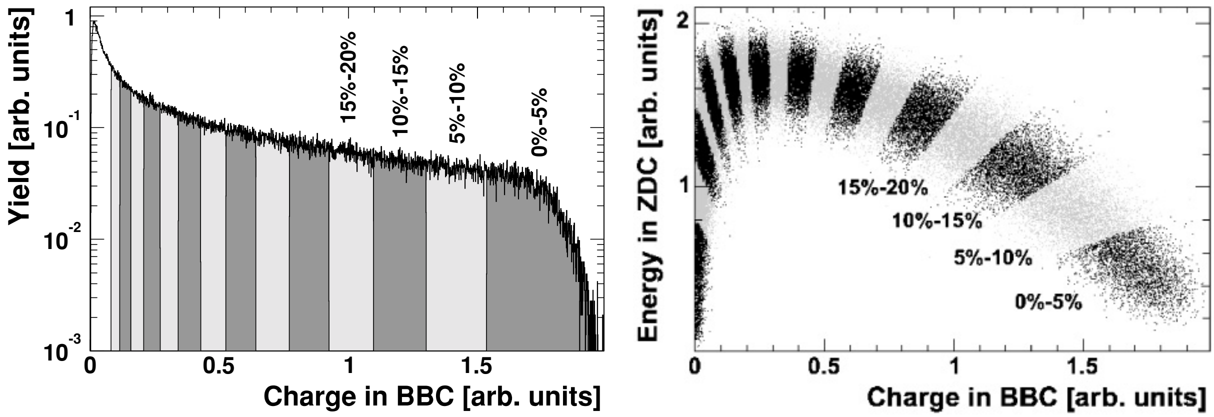

FIG. 1. Different centrality classes based on the BBC (left) and ZDC vs. BBC (right) distributions.

Monte Carlo techniques. To account for the track losses in the real event sample, a correction of 15%, 13%, and 6% for the 5% most central events was applied at $\sqrt{s_{NN}} = 200$, 130, and 19.6 GeV, respectively.

Track losses due to the finite double hit resolution reduce the combinatorial background in the real events more than in the mixed events. The number of tracks in the mixed events must be decreased by 3.6% to account for this. The uncertainty in the correction related to the finite double hit resolution of the PCs was estimated to be 3.5% of the number of reconstructed tracks in the most central events at $\sqrt{s_{NN}} = 200$ GeV. This number was deduced from the simulation and cross-checked with an artificial 50% increase of the double hit resolution of PC1 and PC3.

An additional correction is related to the decay of charged particles and feed-down from the decay of neutral particles. This correction is discussed in [8], where it was determined using the HIJING event generator. In this paper the measured composition of the produced particles at different centralities is used at $\sqrt{s_{NN}} = 200$ and 130 GeV [13,16]. The correction related to particle decay varies about $\pm 1\%$ over the full range of measured centralities. In midcentral events it is $-1 \pm 2.9\%$ and $+1 \pm 2.5\%$ at 200 and 130 GeV, respectively. At the lowest RHIC energy the correction is based on NA49 [17–19] measurements at close energy 17.2 GeV and is about $11 \pm 5.7\%$ independent of centrality. The difference between 19.6 and 130 GeV arises from the decrease of the particle momenta and the width of the η distribution at lower energy which affects the number of tracks from the decay of particles coming from adjacent rapidities. The uncertainty is also larger because the correction was based on non-PHENIX data. More details on the analysis can be found in [8,11,12].

C. Determination of trigger efficiency and N_p

The distribution of the number of participants (N_p) in Au + Au collisions was determined using a Monte Carlo simulation based on the Glauber model. The inelastic cross section of $p + p$ collisions used in the Glauber model was taken to be 31, 41, and 42 mb at $\sqrt{s_{NN}} = 19.6$, 130, and 200 GeV, respectively [20], and was varied within ± 3 mb in order to get the systematic errors. The nuclear density profile $\rho(r)$ was taken as the Woods-Saxon parametrization,

$$\rho(r) = 1/(1 + e^{(r-r_n)/d}), \tag{2}$$

where r_n is the nucleus radius and d is a diffuseness parameter. Based on the measurements of electron scattering from Au nuclei [21], r_n was set to (6.38 ± 0.27) fm and d to (0.54 ± 0.01) fm.

The BBC detectors are located in a region where the number of produced particles is proportional to N_p at $\sqrt{s_{NN}} =$ 130 and 200 GeV [22]. By comparing measured BBC spectra to simulations, the MB trigger efficiency was estimated to be $92.2^{+2.5}_{-3.0}\%$ at both 200 and 130 GeV, with less than 1% uncertainty in the difference between these two energies.

One can also use the BBC (or ZDC vs. BBC) response to define centrality for a given event as a percentage of the total geometrical cross section. The BBC amplitude distribution and ZDC vs. BBC signals divided into centrality classes are shown in Fig. 1.

By matching the detector response simulation to the data, N_p can be assigned to each centrality class. The results for N_p vary by less than 0.5% depending on the shape of the cut in the ZDC/BBC space and whether the BBC alone was used as a centrality measure. The larger error in N_p comes from model uncertainties and can be parametrized as $\Delta N_p/N_p = 0.02 + 3.0/N_p$.

At $\sqrt{s_{NN}} = 19.6$ GeV, the BBC acceptance partially covers the Au nuclei fragmentation region where the relation between the particle production and N_p is not well known for peripheral events. This makes the MB trigger efficiency model dependent. To avoid this problem, an approach based on the Glauber model and the negative binomial distribution (NBD) was applied to the data from the PHENIX central arm. For the centrality associations, the BBC signal can still be used after applying the following correction.

The NBD, written as

$$P(n, \mu, k) = \Gamma(n + k)/(\Gamma(k)n!) \cdot (\mu/k)^n/(1 + \mu/k)^{n+k}, \tag{3}$$

represents the number of independent trials n that are required to get a number of predetermined successes if the average number of successes per trial is μ. The parameter k is related

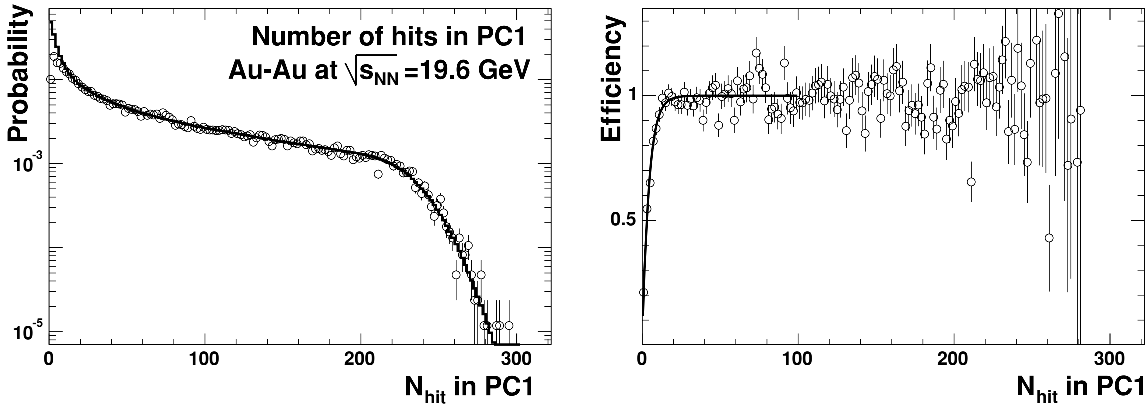

FIG. 2. Left panel: Glauber/NBD fit (line) to the distribution of the number of hits in the PC1 detector at $\sqrt{s_{NN}} = 19.6$ GeV (circles). Right panel: MB trigger efficiency as a function of the number of hits. The parametrization is to guide the eye.

to the variance of the distribution by the equation $(\sigma/\mu)^2 = 1/k + 1/\mu$. By associating n with the number of particles produced in the event such that $n = f(N_p)$, the NBD describes the distribution of hits in a detector [23,24] produced by a given number of N_p. In the simplest case when $n \propto N_p$, $\langle N_{\rm hit}\rangle = \mu\langle N_p\rangle$. Using probability weights for N_p from the Glauber model, one can construct a distribution of the number of hits in a detector. The coefficients μ and k can be obtained by fitting the constructed distribution to the experimentally measured distribution.

The number of hits in the PC1 detector shown in the left panel of Fig. 2 was used to determine the trigger efficiency. $N_{\rm hit} \propto dN_{\rm ch}/d\eta$ can be parametrized as scaling with the number of participants N_p^{α}, where α is between 1.0 and 1.1 as measured by WA98 at the CERN SPS [25]. The Glauber/NBD fit to the distribution of the number of hits in PC1 is shown as the solid line. The fitting range is constrained above some number of hits, where the trigger efficiency is equal to 1. The efficiency as a function of the number of hits in the detector can be found by taking the ratio of measured and reconstructed distributions. This is shown in the right panel of Fig. 2. Intergated over all $N_{\rm hits}$ the MB trigger efficiency was found to be $81.5 \pm 3\%$ at $\sqrt{s_{NN}} = 19.6$ GeV. The 1% uncertainty due to variation of α from 1.0 to 1.1 was included in the systematic error. An uncertainty in the difference between 19.6 and 200 GeV was 1.5%.

A fraction of events missing in the trigger at all energies belongs to the peripheral centrality classes outside the centrality range discussed in this paper.

As a cross-check, the same procedure was applied to the BBC response at 200 GeV. It was found that the MB trigger efficiency in Au + Au and d + Au collisions agrees with the procedure based on a full simulation within one standard deviation of the systematic error. In Au + Au the N_p in the centrality bins determined using the Glauber/NBD method agree better than 0.5% with the values used in this paper. In d + Au for a single nucleon-nucleon collision the MB trigger efficiency was found to be 57%, consistent with the $52 \pm 7\%$ measured for PHENIX $p + p$ trigger efficiency at the same energy using a different method [26]. Finally, the fraction of expected p + Au collisions in the d + Au sample agrees with the fraction of events in which the corresponding ZDC detects the spectator neutron from the deuteron within better than 1.5%.

As stated above, the BBC detector at $\sqrt{s_{NN}} = 19.6$ GeV covers a part of the Au nuclei fragmentation region, and its response is not linear with N_p [22]. Also, the number of hits in BBC has a strong vertex dependence mainly because the BBC samples different parts of the $dN_{\rm ch}/d\eta$ distribution at different vertices; see Fig. 3. The asymmetry of north and south BBC amplitudes in the same event was studied to correct for these two effects. Around vertex $z = 0$ the asymmetry between the number of hits in north BBC $N(z)$ and south BBC $S(z)$ is $(N(z) - S(z))/(S(z) + N(z)) \propto (d^2N_{\rm ch}/d\eta^2)/(dN_{\rm ch}/d\eta)$ reflects the slope of the η distribution at BBC rapidity. To use the BBC signal for the N_p determination, the observed signals were scaled such that the asymmetry between north and south was the same as in the most central events where the influence of the fragmentation region was negligible. The data were also corrected for vertex dependence. The results of the correction are shown in Fig. 3.

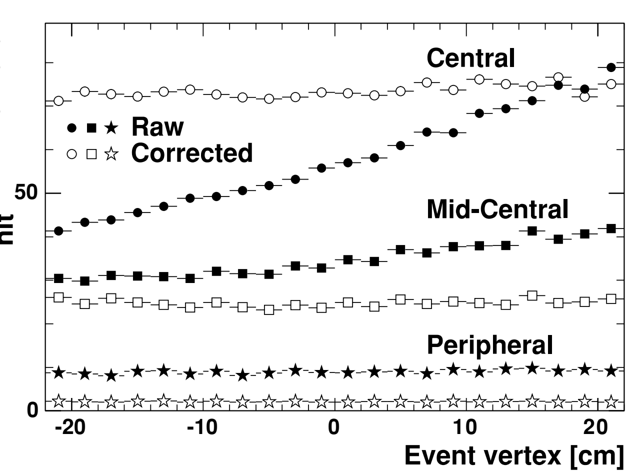

FIG. 3. Average number of hits in BBC north vs. event vertex at different centralities before correction (solid symbols) and after correction (open symbols).

TABLE I. Summary of systematic errors given in percent. When a range is given, the first number corresponds to the most central bin and the second to the most peripheral bin presented in Appendix B, Tables XIII–XV.

	$dE_T/d\eta$			$dN_{\mathrm{ch}}/d\eta$		
$\sqrt{s_{NN}}$ (GeV)	19.6	130	200	19.6	130	200
Energy resp.	4.7	3.8	3.9			
Bkg./noise	0.5–3.5	0.4–10	0.2–6	1.0	1.0	1.0
Acceptance	2.0	2.0	2.0	2.3	2.5	2.3
In- & outflow	3.0	3.0	3.0	5.7	2.5	2.9
Occupancy				1.6–0.3	3.1–0.1	3.5–0.1
Centrality	2.0	0.5	0.5		Same	
N_p	2.9–6.7	2.8–15	2.8–15		Same	
Trigger	0.4–8.8	0.3–16	0.3–16		Same	

The corrected BBC response was used for the centrality determination. Based on both data and Monte Carlo simulation, a systematic error of 2% was added to the determination of the centrality classes using the BBC correction procedure.

D. Systematic error summary

Table I summarizes the systematic errors discussed in this section. The “Energy resp.” error for the E_T measurements combines the uncertainties in absolute energy scale, hadronic response, and energy losses on the EMCal edges and from energy thresholds. The resulting error for each centrality bin is a quadratic sum of the errors listed in the table.

IV. RESULTS

A. PHENIX results

The distribution of the raw transverse energy $E_{T_{\mathrm{EMC}}}$ into the fiducial aperture of two EMCal sectors is shown in the left three panels of Fig. 4 for the three RHIC energies. The lower scale represents the fully corrected E_T normalized to one unit of pseudorapidity and full azimuthal acceptance. The lower axis in the plot is not labeled beyond 200 GeV to avoid confusion between the true shape of the $dE_T/d\eta$ distribution and E_T as measured using the limited acceptance of two EMCal sectors.

For the measurements at $\sqrt{s_{NN}} = 19.6$ and 200 GeV, five EMCal sectors (with azimuthal coverage $\Delta\phi = 112^\circ$) were used, while only two sectors ($\Delta\phi = 45^\circ$) were available during

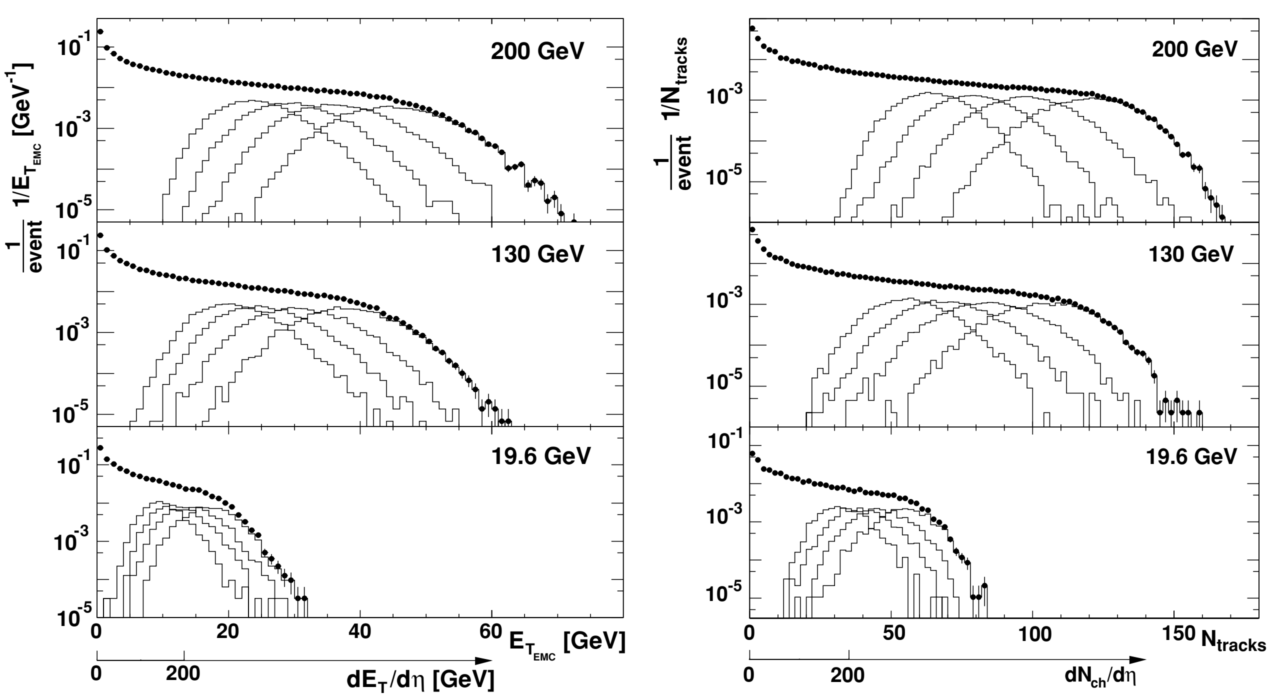

FIG. 4. The distribution of the raw E_T in two EMCal sectors (left) and the number of tracks in the east arm of the PHENIX detector (right) per MB trigger, measured at three energies. The lower axis corresponds to midrapidity values of $dE_T/d\eta$ and $dN_{\mathrm{ch}}/d\eta$, respectively. Distributions of the four 5% most central bins are also shown in each plot.

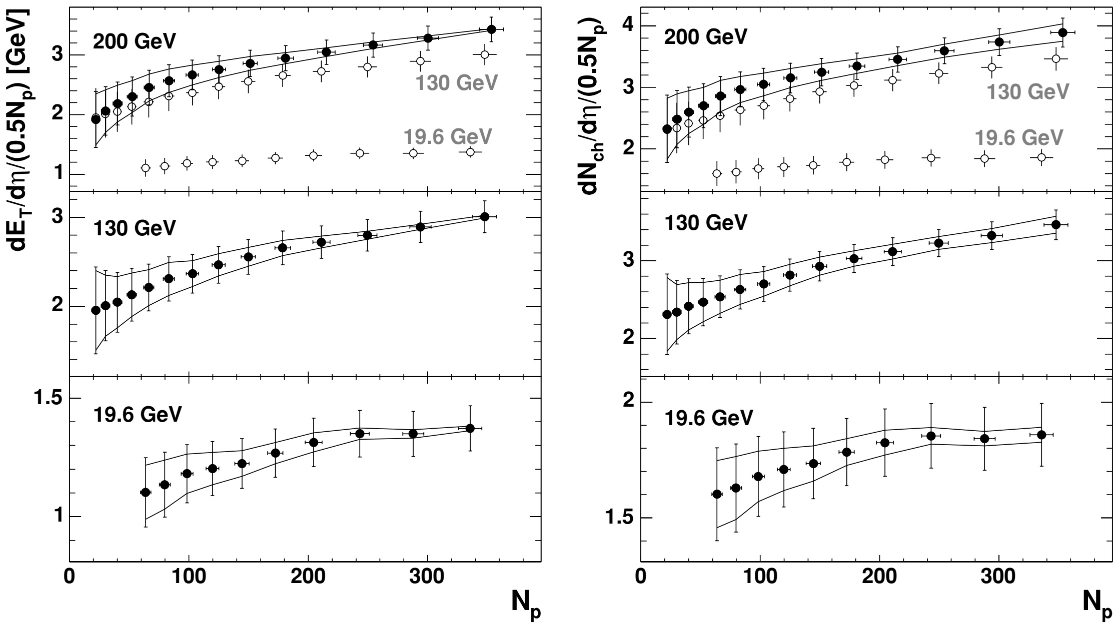

FIG. 5. $dE_T/d\eta$ (left) and $dN_{\mathrm{ch}}/d\eta$ (right) divided by the number of participant pairs at three RHIC energies. Errors shown with vertical bars are full systematic errors. Lines show the part of the systematic error that allows bending or inclination of the points. Horizontal errors denote the uncertainty in determination of N_p.

the PHENIX run at 130 GeV. Results obtained with different number of sectors at the same energy were consistent within 1.5%.

The right three panels in Fig. 4 show the number of tracks reconstructed in the east arm of the PHENIX detector after background subtraction and all corrections. The lower axis corresponds to measured distributions normalized to one unit of pseudorapidity and full azimuthal acceptance. For a similar reason as for the E_T measurement, the lower axis is not labeled above 200 GeV in $dN_{\mathrm{ch}}/d\eta$.

For the N_{ch} measurements at $\sqrt{s_{NN}} = 130\,\mathrm{GeV}$, only the east arm was used; for the other two energies the measurements were made using both PHENIX central arms. The results obtained with two arms at 200 and 19.6 GeV are consistent with each other within 1.5%.

The distributions shown in Fig. 4 have a characteristic shape with a sharp peak that corresponds to the most peripheral events. Missing events caused by the finite MB trigger efficiency in peripheral events would make this peak even sharper than measured. The plateau in all distributions corresponds to midcentral events, and the falloff to the most central Au + Au events. The shape of the curves in Fig. 4 in the falloff region is a product of the intrinsic fluctuations of the measured quantities and the limited acceptance of the detector.

The distributions for the four most central bins (0–5% to 15–20%) are also shown in each panel. The centroids of these distributions were used to calculate the centrality dependence of $dE_T/d\eta$ and $dN_{\mathrm{ch}}/d\eta$.[3] The statistical uncertainties of all mean values (less than or about 1%) determined by the width of the distributions are small because of the large size of the event samples.

The magnitude of $dE_T/d\eta$ and $dN_{\mathrm{ch}}/d\eta$ at midrapidity divided by the number of participant pairs as a function of N_p is shown in Fig. 5 and tabulated in Appendix B, Tables XIII–XV. The right three panels show the same ratio for $dN_{\mathrm{ch}}/d\eta$ at the three RHIC energies.

The horizontal errors correspond to the uncertainty in N_p, determined within the framework of the Monte Carlo–Glauber model. The vertical bars show the full systematic errors of the measurements[4] added quadratically to the errors of N_p. The lines denote the corridor in which the points can be inclined or bent. The statistical errors are smaller than the size of the markers. The upper panel also shows the results of the two lower panels with open markers for comparison.

An important result from Fig. 5 is an evident consistency in the behavior of the centrality curves of E_T shown on the left and N_{ch} shown on the right for all measured energies. Both values demonstrate an increase from peripheral (65–70% bin) to the most central events by 50–70% at RHIC energies 130 and 200 GeV. For the lowest RHIC energy (19.6 GeV) this increase is at the level of systematic uncertainties of the measurement. One can note that results from PHOBOS [27] show that the total charged particle multiplicity is proportional to N_p, while the multiplicity at midrapidity over N_p increases with N_p, indicating that the pseudorapidity distribution gets more narrow for central events.

The ratios of the $dE_T/d\eta$ and $dN_{\mathrm{ch}}/d\eta$ per participant pair measured at different RHIC energies are shown in

[3]All plotted and quoted numbers correspond to average values in each centrality bin or ratios of those averages.

[4]Here and everywhere errors correspond to one standard deviation.

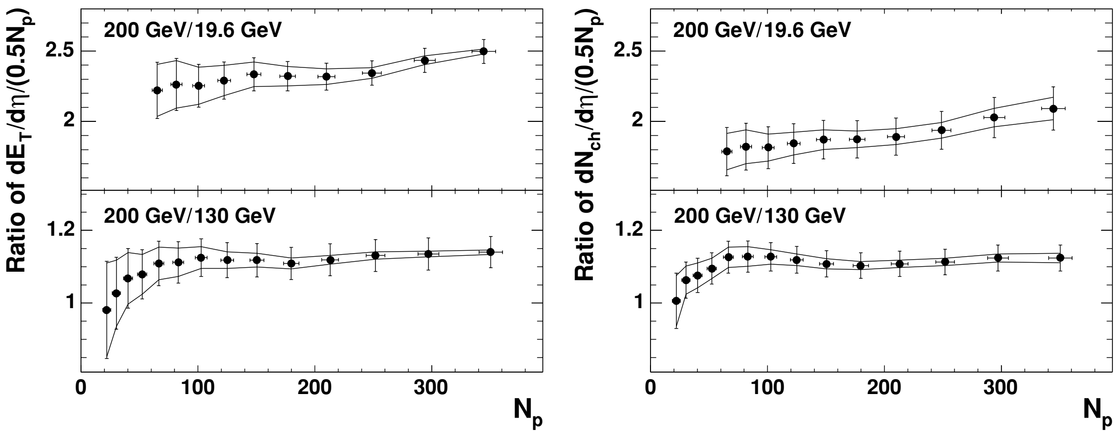

FIG. 6. Same as Fig. 5, but for ratios of $dE_T/d\eta$ (left) and $dN_{ch}/d\eta$ (right) measured at different RHIC energies.

Fig. 6 and tabulated in Table XVI. In these ratios some common systematic errors cancel.

The increase in the E_T production between 19.6 and 200 GeV (with an average factor of 2.3) is larger than for N_{ch} (with average factor of 1.9). This is consistent with an increase in the particle production per participant common to both E_T and N_{ch} and a $\sim$20% increase in $\langle m_T \rangle$ of produced particles contributing to the E_T parameter only. See Appendix A 1 and [16,17].

The ratio of 200/19.6 GeV shows some increase from peripheral to central events; however, the increase is marginally at the level of the systematic errors of the measurement.

The ratio of 200/130 GeV is flat above $N_p \sim 80$ and is equal to 1.140 ± 0.043 for E_T and 1.126 ± 0.036 for N_{ch} in the most central bin. A rather sharp increase between $N_p = 22$ and 83 in the ratios of both quantities is still at the level of systematic uncertainties.

The ratio of the transverse energy and charged particle multiplicity at midrapidity as a function of centrality is shown in Fig. 7 for the three energies. The upper plot also shows the results displayed in the lower panels for comparison.

The ratio E_T/N_{ch},[5] sometimes called the "global barometric observable," triggered considerable discussion [28,29]. It is related to the $\langle m_T \rangle$ of the produced particles and is observed to be almost independent of centrality and incident energy of the collisions within the systematic errors of the previous measurements. The present paper forges a direct link between the highest SPS and lowest RHIC energies, making a more quantitative study of E_T/N_{ch} possible.

The results presented in Fig. 7 and tabulated in Tables XIII–XV show that the centrality dependence of E_T/N_{ch} is weak and lies within the systematic errors plotted with lines. There is a clear increase in E_T/N_{ch} between $\sqrt{s_{NN}} = 19.6$ and 200 GeV. The $\sqrt{s_{NN}}$ dependence of the results is discussed below.

B. Bjorken energy density

The Bjorken energy density [30] can be calculated using

$$\epsilon_{Bj} = \frac{1}{A_\perp \tau} \frac{dE_T}{dy}, \tag{4}$$

where τ is the formation time and $A_\perp$ is the nuclei transverse overlap area.

The transverse overlap area of two colliding nuclei was estimated using a Monte Carlo–Glauber model $A_\perp \sim \sigma_x \sigma_y$, where σ_x and σ_y are the widths of x and y position distributions of the participating nucleons in the transverse plane. The normalization to πR^2, where R is the sum of r_n and d parameters in a Woods-Saxon parametrization [Eq. (2)], was done for the most central collisions at the impact parameter $b = 0$. For the transformation from $dE_T/d\eta|_{\eta=0}$ to $dE_T/dy|_{y=0}$, a scale factor of 1.25 ± 0.05 was used; see Appendix A 1.

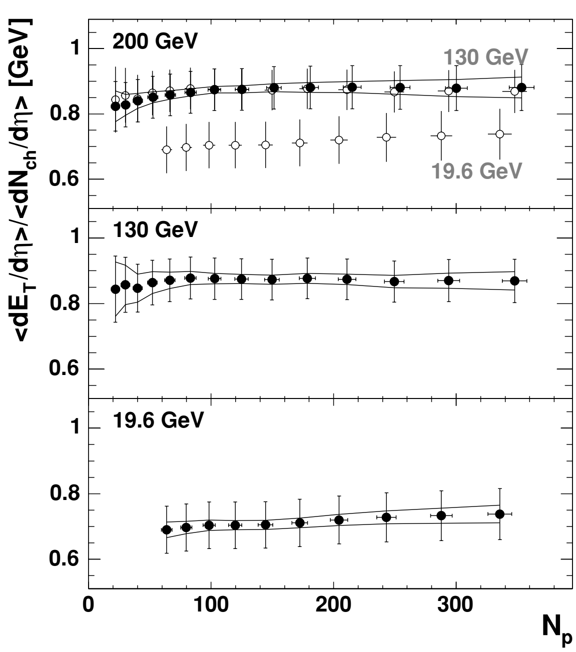

FIG. 7. Same as Fig. 5, but for E_T/N_{ch} vs. N_p at different RHIC energies.

[5] E_T/N_{ch} is used as a shortcut for $\langle dE_T/d\eta \rangle / \langle dN_{ch}/d\eta \rangle$ at $\eta = 0$ in the c.m. system.

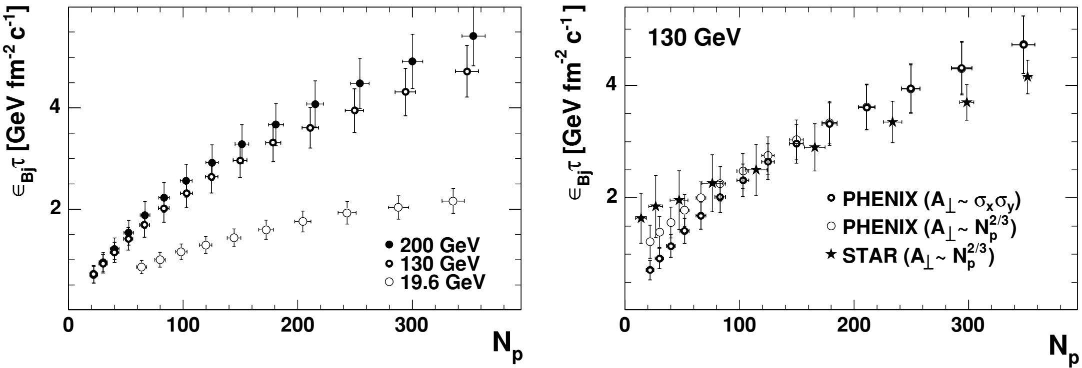

FIG. 8. $\epsilon_{Bj} \cdot \tau$ deduced from the PHENIX data at three RHIC energies (left) and using different estimates of the nuclear transverse overlap at $\sqrt{s_{NN}} = 130$ GeV (right).

The Bjorken energy density for three RHIC energies is plotted in the left panel of Fig. 8 and tabulated in Tables XIII–XV. For the 5% most central collisions, $\epsilon_{Bj} \cdot \tau$ was $2.2 \pm 0.2, 4.7 \pm 0.5$, and 5.4 ± 0.6 GeV fm$^{-2}c^{-1}$ for $\sqrt{s_{NN}} =$ 19.6, 130, and 200 GeV, respectively. These values increase by 2, 4, and 5%, respectively, for the maximal $N_p = 394$, as obtained from extrapolation of PHENIX data points. There is a factor of 2.6 increase between the SPS-like energy (19.6 GeV) and the top RHIC energy (200 GeV). The comparison of the only published $\epsilon_{Bj} = 3.2$ GeV/fm^3 at SPS for head-on collisions [31] and top RHIC energies, assuming the same $\tau = 1$ fm/c, reveals an increase in energy density by a factor of only 1.8, which may come from an overestimation in the SPS measurement, as shown latter in the left panel of Fig. 13 and discussed in Appendix A 3.

Another approach is used by STAR in [32] for the estimate of the transverse overlap area of the two nuclei $A_\perp \sim N_p^{2/3}$ in Eq. (4). This approach accounts for only the common area of colliding nucleons, not nuclei. The results are different only in the peripheral bins as shown in the right panel of Fig. 8. For a comparison, the same panel shows the result obtained by STAR which agrees with PHENIX results within systematic errors, though displaying a smaller increase of the energy density with N_p.

C. Comparison to other measurements

Comparison to the results of other experiments is complicated by several factors. AGS and SPS data were taken in the laboratory (Lab.) system while the RHIC data are in the center-of-mass system (c.m.s.). Since η and E_T are not boost-invariant quantities, the data should be converted into the same coordinate system. Some experiments provide a complete set of identified particle spectra from which information about E_T and N_{ch} can be deduced. For other experiments, additional assumptions are necessary for their published values. Appendix A describes how such recalculation was done in each particular case.

The PHENIX results for N_{ch} are compared to the data available from the other RHIC experiments. This comparison is shown in the left panels of Fig. 9.

There is good agreement between the results of BRAHMS [33,34], PHENIX, PHOBOS [35–37], and STAR [38,39] using N_p based on a Monte Carlo–Glauber model. This agreement is very impressive because all four experiments use different apparatuses and techniques to measure the charged particle production. The systematic errors of all results are uncorrelated, except for those related to the same Glauber model, which are small. That makes it possible to calculate the RHIC average and reduce the systematic uncertainty. The averaged results from all four RHIC experiments are plotted in the right panel of Fig. 9 and tabulated in Table XVII. See Appendix A 2 for the procedure.

Figure 10 compares E_T results from the PHENIX and STAR [40] experiments. The results are consistent for all centralities within systematic errors, though the STAR $dE_T/d\eta$ per participant pair has a smaller slope vs. N_p above ~70 participants, and E_T/N_{ch} shown in the lower panel is consistent for all N_p.

The RHIC run at $\sqrt{s_{NN}} = 19.6$ GeV allows a connection between RHIC and SPS data to be made. The highest SPS energy per projectile nucleon of 158 A GeV corresponds to $\sqrt{s_{NN}} = 17.2$ GeV in the c.m.s., making a direct comparison of RHIC and SPS results possible. This comparison is shown in Fig. 11. See Appendixes A 3–A 6 for the details of the data compilation.

Several comments should be made about this comparison. For both measured parameters the PHENIX results and the SPS results agree. The WA98 results (see Appendix A 4) are systematically higher than the results of other experiments, especially for $dE_T/d\eta$. However, the WA98 data have an additional systematic error common to all points shown for the last bin. For N_{ch} the relative spread of the SPS results is larger than for the RHIC results shown in Fig. 9, though overall the $\sqrt{s_{NN}} = 17.2$ GeV SPS measurements are consistent with the PHENIX result at 19.6 GeV.

Different SPS and AGS experiments made measurements at lower energies. The combined data of AGS, SPS, and RHIC provide a complete picture of the centrality behavior of E_T and N_{ch} as a function of the nucleon-nucleon energy. The centrality dependence of $dN_{ch}/d\eta$ at midrapidity measured at $\sqrt{s_{NN}} =$ 4.8, 8.7, and 17.2 GeV by different experiments is shown in Fig. 12. See Table XVII for the summary of these results and Appendixes A 5–A 7 for the details of the data compilation.

At the highest SPS energy the averaging procedure is the same as for RHIC energies, and weighted experimental errors are

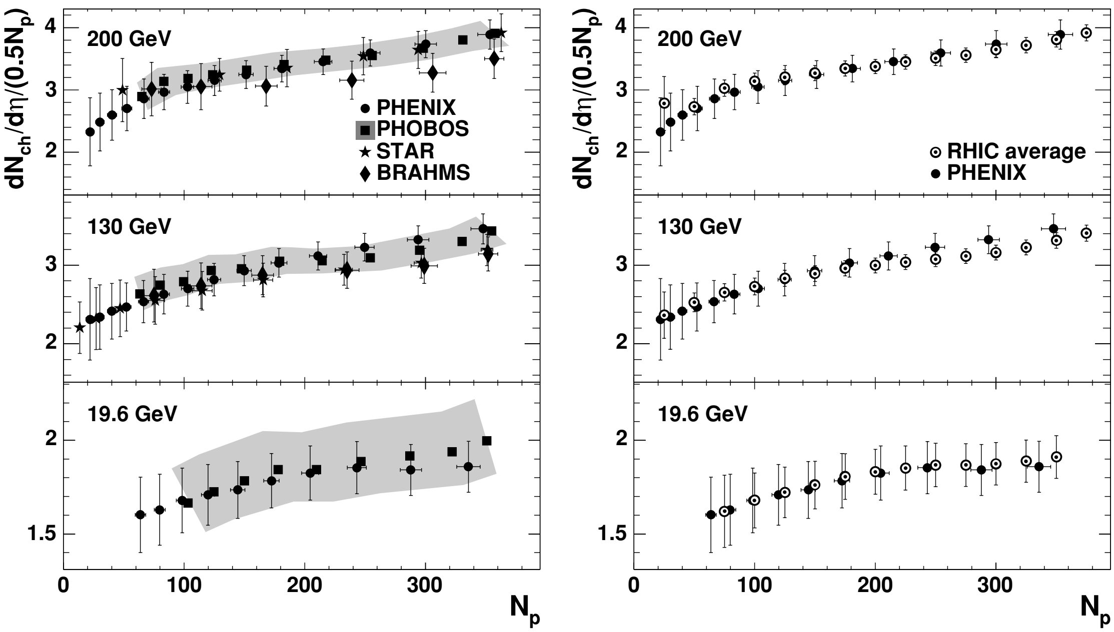

FIG. 9. Left panel: $dN_{ch}/d\eta$ per pair of N_p measured by the four RHIC experiments at different energies. The shaded area is the PHOBOS systematic error. Right panel: RHIC average values (including PHENIX) compared to the PHENIX results.

scaled with the reduced χ^2-like factor S (described in Appendix A 2) reaching the value of 1.5 at some points. For the intermediate SPS energy $\sqrt{s_{NN}} = 8.7$ GeV, two experiments, NA45 [41] and NA50 [42], reported the centrality dependence of $dN_{ch}/d\eta$ at midrapidity. The discrepancy in the measurements is close to three times the quadratic sum of their systematic error. However, the shapes of the two curves are almost the same. NA49 has published results (see Appendix A 3) that give one point in $dN_{ch}/d\eta$ at $N_p = 352$. This point favors the NA45 result.[6]

[6]The NA57 results at both SPS energies are published without systematic errors in [43] They are currently not considered.

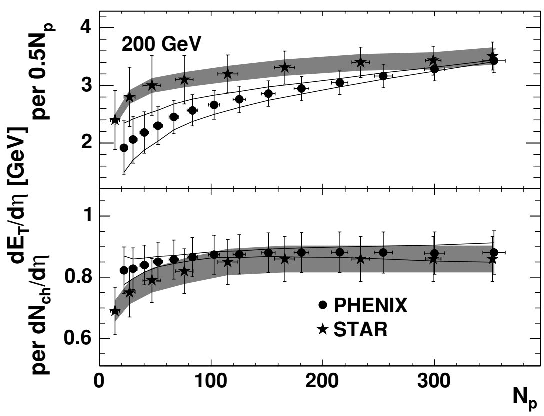

FIG. 10. $dE_T/d\eta$ divided by the number of N_p pairs (top) and E_T/N_{ch} (bottom) measured by the PHENIX and STAR [40] experiments at $\sqrt{s_{NN}} = 200$ GeV. PHENIX systematic errors are explained in the text. The shaded area is the STAR systematic scaling error.

The average centrality curve is produced taking into account the shape of the centrality curves reported by NA45 and NA50 and the single NA49 point. See Appendix A 8 for the averaging procedure at $\sqrt{s_{NN}} = 8.7$ GeV. The errors are scaled with the factor S, which reaches a value of 2.5 at some points. The AGS results are presented with a curve produced from the combined results of the E802/E917 experiments (see Appendix A 7). The averaging procedure in this case is a simple rebinning of the data.

The average SPS centrality dependence at $\sqrt{s_{NN}} = 17.2$ GeV shown in the upper panel in Fig. 12 and the average curve of the two RHIC experiments at 19.6 GeV shown in the lower panel in Fig. 9 are very similar. Less than a 5% increase is expected to result from the difference in the incident energy between the highest SPS and the lowest RHIC energies (see Sec. IV D below). The average values presented in Figs. 9 and 12 are summarized in Table XVII.

D. Dependence on the incident nucleon energy

The data compilation made in the previous section allows for a detailed study of the charged particle production in heavy ion reactions at different incident energies of colliding nuclei. Although the data on transverse energy production are not abundant, a similar comparison can be made [9,10].

1. Central collisions

Figure 13 shows the energy dependence of the $dE_T/d\eta$ and $dN_{ch}/d\eta$ production per pair of participants in the most central collisions measured by different experiments. See Appendixes A 5–A 9 for the details of the data compilation.

The results shown in Fig. 13 are consistent with logarithmic scaling as described in [9,11,12]. Use of the logarithmic

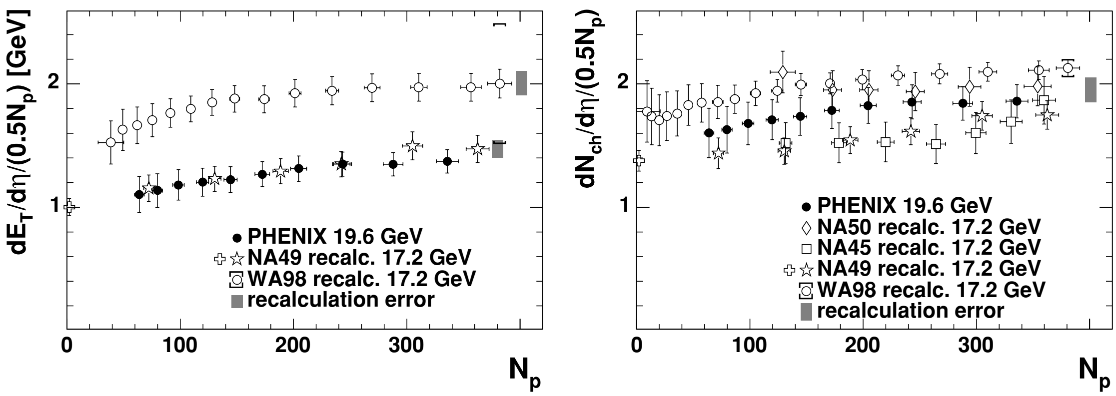

FIG. 11. $dE_T/d\eta$ (left) and $dN_{\rm ch}/d\eta$ (right) divided by the number of N_p pairs measured by PHENIX at $\sqrt{s_{NN}} = 19.6$ GeV (solid markers) and recalculated from the results of the SPS experiments at the highest energy $\sqrt{s_{NN}} = 17.2$ GeV (open markers). The $p + p$ result of NA49 is marked with an open cross.

function is phenomenological and is suggested by the trend of the data in the range of available measurements. The agreement of the fits with the data in both panels is very good, especially in the right panel where the averaged values are used for $N_p = 350$. The single point of NA49 [31] is excluded from the E_T fit (see Appendix A 3). The results of the fit $dX/d\eta = (0.5N_p \cdot A)\ln(\sqrt{s_{NN}}/\sqrt{s_{NN}^0})$ are

for E_T, $\sqrt{s_{NN}^0} = 2.35 \pm 0.2$ GeV and $A = 0.73 \pm 0.03$ GeV,
for $N_{\rm ch}$, $\sqrt{s_{NN}^0} = 1.48 \pm 0.02$ GeV and $A = 0.74 \pm 0.01$.

The parameter $\sqrt{s_{NN}^0} = 2.35$ GeV obtained from the E_T fit is slightly above although within 3σ from the minimum possible value of $\sqrt{s_{NN}} = 2 \times \text{amu} = 1.86$ GeV. The measurement closest to it at $\sqrt{s_{NN}} = 2.05$ GeV done by the FOPI experiment allows one to estimate the amount of $dE_T/d\eta$ produced to be 5.0 GeV in the most central collisions corresponding to $N_p = 359$. Appendix A 9 gives details of the estimate. This does not disagree with the extrapolation of the fit but does indicate that the logarithmic parametrization requires higher order terms to describe how the E_T production starts at very low $\sqrt{s_{NN}}$.

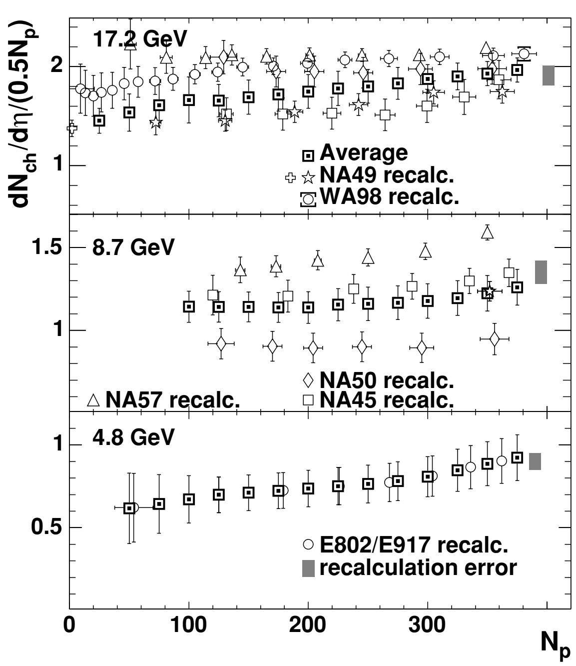

FIG. 12. $dN_{\rm ch}/d\eta$ divided by the number of N_p pairs measured by AGS and SPS experiments and the average taken at different energies recalculated in the c.m.s.

The right panel of Fig. 13 shows the logarithmic fit to the $N_{\rm ch}$ data. It agrees well with all $dN_{\rm ch}/d\eta$ results plotted for $N_p = 350$. Unlike that for E_T, the fit parameter $\sqrt{s_{NN}^0}$ for $N_{\rm ch}$ is 1.48 ± 0.02 GeV which is lower than the minimum allowed $\sqrt{s_{NN}}$. This suggests that above $2 \times$ amu the $N_{\rm ch}$ production as a function of $\sqrt{s_{NN}}$ should undergo threshold-like behavior, unlike the E_T production which must approach zero smoothly because of energy conservation.

The FOPI measurements at $\sqrt{s_{NN}} = 1.94$ and 2.05 GeV agree with the extrapolation of the fit at energy very close to $2 \times$ amu. It is an interesting result that colliding nuclei with kinetic energies of 0.037 and 0.095 GeV per nucleon in the c.m.s. follow the same particle production trend as seen at AGS, SPS, and RHIC energies.

A fit to the charged particle multiplicity shows a factor of 2.2 increase in $dN_{\rm ch}/d\eta$ per participant in the most central events from the highest energy at the AGS ($\sqrt{s_{NN}} = 4.8$ GeV) to the highest energy at the SPS (17.2 GeV) and a factor of 2.0 from the highest SPS energy to the highest RHIC energy (200 GeV). Assuming the same behavior extends to the Large Hadron Collider (LHC) highest energy (5500 GeV) one would expect $dN_{\rm ch}/d\eta = (6.1 \pm 0.13) \cdot (0.5N_p)$ and the increase in particle production from the highest RHIC energy to be $\sim$60% for the most central events. With the greater energy, the rapidity width should increase by $\sim$60%, i.e., the total charged particle multiplicity at LHC would increase by a factor of $\sim$2.6 from the top RHIC energy.

The ratio of $E_T/N_{\rm ch}$ for the most central bin as a function of $\sqrt{s_{NN}}$ is shown in Fig. 14. Note that the line shown in the figure is not the fit to the data points. Rather, it is calculated from the fits shown in Fig. 13. The calculation agrees well with the data. There are two regions in the plot which can be clearly separated. The region from the lowest allowed $\sqrt{s_{NN}}$ to SPS energy is characterized by a steep increase of

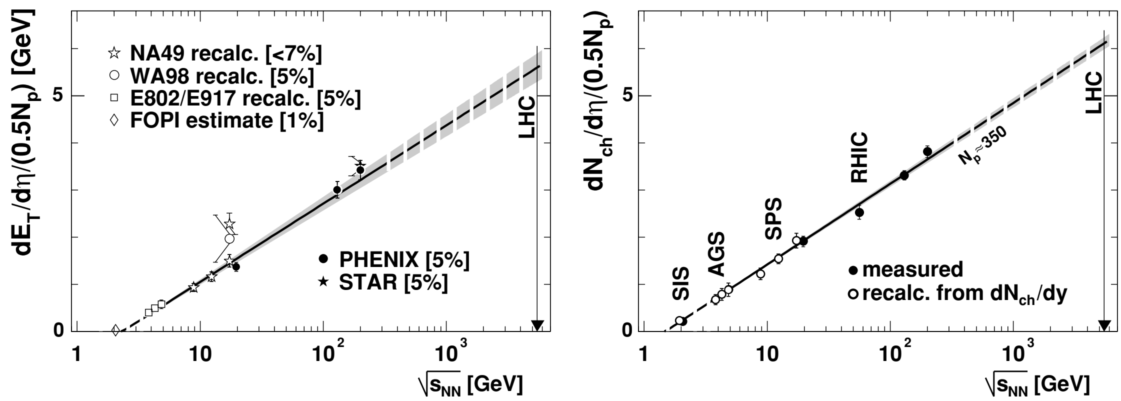

FIG. 13. Left panel: $dE_T/d\eta$ divided by the number of N_p pairs measured in the most central bin (value given in brackets) as a function of incident nucleon energy. The line is a logarithmic fit. The band corresponds to a 1σ statistical deviation of the fit parameters. Right panel: the same for $dN_{\rm ch}/d\eta$. The values of $N_{\rm ch}$ are the average values corresponding to $N_p = 350$. The single point at $\sqrt{s_{NN}} = 56$ GeV is explained in Appendix A 10.

the $E_T/N_{\rm ch}$ ratio with $\sqrt{s_{NN}}$. In this region the increase in the incident energy causes an increase in the $\langle m_T \rangle$ of the produced particles. The second region starts from the SPS energies and continues above. In this region, the $E_T/N_{\rm ch}$ ratio is very weakly dependent on $\sqrt{s_{NN}}$. The incident energy is converted into particle production at midrapidity rather than into increasing the particle $\langle m_T \rangle$.

The shape of the $E_T/N_{\rm ch}$ curve in the first region is governed by the difference in the $\sqrt{s^0_{NN}}$ parameter between E_T and $N_{\rm ch}$. In the second region it is dominated by the ratio of the A parameters in the fits. This ratio is close to 1 GeV. Extrapolating to LHC energies one gets a $E_T/N_{\rm ch}$ value of (0.92 ± 0.06) GeV.

2. Centrality shape

Another interesting question is how the shapes of the centrality curves of E_T and $N_{\rm ch}$ change with $\sqrt{s_{NN}}$.

One approach previously used in a number of papers is to describe the shape of the centrality dependence as a sum of "soft" and "hard" contributions such that the soft component is proportional to N_p and the hard component to the the number of binary collisions N_c, that is, $A \times N_p + B \times N_c$. A disadvantage of this approach is that the contributions called soft and hard do not necessarily correspond to the physical processes associated with these notations. Another approach is to assume that the production of E_T or $N_{\rm ch}$ is proportional to N_p^α, although the parameter α has no physical meaning.

The results of B/A and α obtained from the fits to the data at different $\sqrt{s_{NN}}$ are summarized in Table II. Although the numbers tend to increase with beam energy, the values presented in Table II are consistent with each other within the systematic errors.

The availability of higher quality data would make it possible to derive a more conclusive statement about the shape of the curves plotted in Figs. 9 and 12. With the present set of data usually limited to N_p above 50, a large part of the

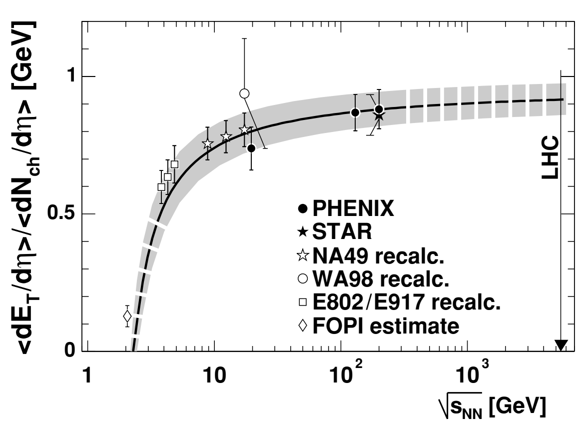

FIG. 14. Ratio of E_T over $N_{\rm ch}$ for the most central events as a function of $\sqrt{s_{NN}}$ recalculated into c.m.s. The line is the ratio of two fits shown in Fig. 13. The band corresponds to one standard deviation of the combined error.

TABLE II. B/A ratio and parameter α from the fit to the data. Errors are calculated assuming a change in the slope of the centrality curves within the limits of the bending errors for PHENIX and full errors for the averaged data (Table XVII).

$\sqrt{s_{NN}}$ (GeV)	$dE_T/d\eta$ PHENIX	$dN_{\rm ch}/d\eta$ PHENIX	$dN_{\rm ch}/d\eta$ Average
		B/A	
200	$0.49^{+.69}_{-.22}$	$0.41^{+.57}_{-.21}$	$0.28^{+.18}_{-.15}$
130	$0.41^{+.52}_{-.23}$	$0.41^{+.45}_{-.23}$	$0.26^{+.18}_{-.11}$
19.6	$0.37^{+.48}_{-.22}$	$0.21^{+.30}_{-.15}$	$0.23^{+.73}_{-.23}$
17.2			$0.31^{+.46}_{-.24}$
8.7			$0.12^{+.64}_{-.20}$
	Parameter α		
200	1.20 ± 0.07	1.18 ± 0.08	1.16 ± 0.06
130	1.14 ± 0.08	1.17 ± 0.08	1.14 ± 0.05
19.6	1.13 ± 0.07	1.09 ± 0.06	1.10 ± 0.11
17.2			1.11 ± 0.08
8.7			1.06 ± 0.13
4.8			1.20 ± 0.24

centrality curve is missing or smeared by systematic errors. To avoid this, one can compare Au + Au collisions to $p + p$ ($N_p = 2$) at the same energy.

Figure 15 shows $dN_{ch}/d\eta/(0.5N_p)$ divided by the parametrization plotted in the right panel of Fig. 13. The top panel shows the most central events with $N_p = 350$. All points are consistent with 1, demonstrating an agreement of the fit to the data. The points are connected with a line for visibility. The middle panel shows results for midcentral events, with $N_p = 100$ connected with a solid line. The dotted line is the same line as in the top panel for $N_p = 350$. The points for $N_p = 100$ are lower than for $N_p = 350$ by a factor of 0.8–0.9, over the plotted range of incident energies. The lower panel shows $p + p$ data corresponding to $N_p = 2$ measured by several experiments. The dotted lines are the same as appear in the upper two panels for $N_p = 350$ and 100, and the $p + p$ parametrizations are taken from [44,45]. In the range of RHIC energies these points are lower by a factor of 0.65–0.75 than the most central events.

These results indicate that the centrality curves normalized to the most central collisions have a similar shape for all RHIC energies within the errors of available measurements.

E. Comparison to models

A variety of models attempting to describe the behavior of E_T and N_{ch} as a function of centrality at different $\sqrt{s_{NN}}$ are available. An updated set of model results were collected from several theoretical groups to make a comparison as comprehensive as possible. Figures 16–18 show the comparison

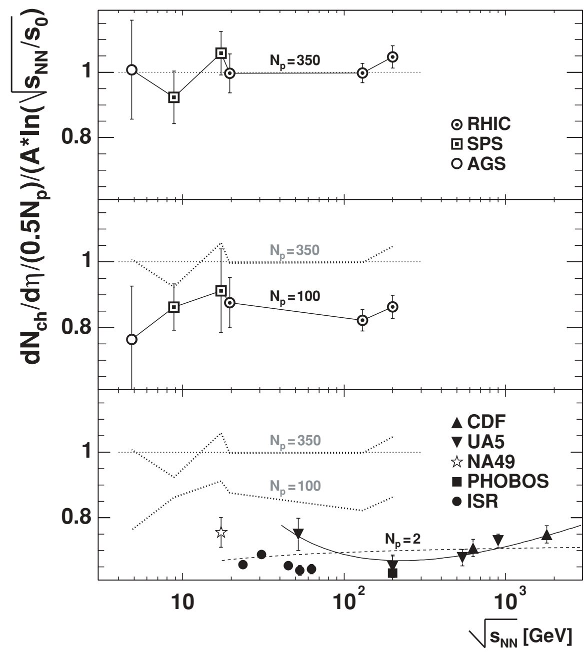

FIG. 15. The three panels show $dN_{ch}/d\eta/(0.5N_p)$ divided by the logarithmic parametrization from Fig. 13. The panels correspond to $N_p = 350$, 100, and 2 ($p + p$) from top to bottom. Au + Au points are connected with lines also shown in lower panels for comparison. The Au + Au data are tabulated in Table XVII. $p + p$ data and parametrizations $dN/d\eta = 2.5 - 0.25\ln(s_{NN}) + 0.023\ln(s_{NN})^2$ (solid line) and $dN/d\eta = 0.27\ln(s_{NN}) - 0.32$ (dashed line) are taken from [44,45].

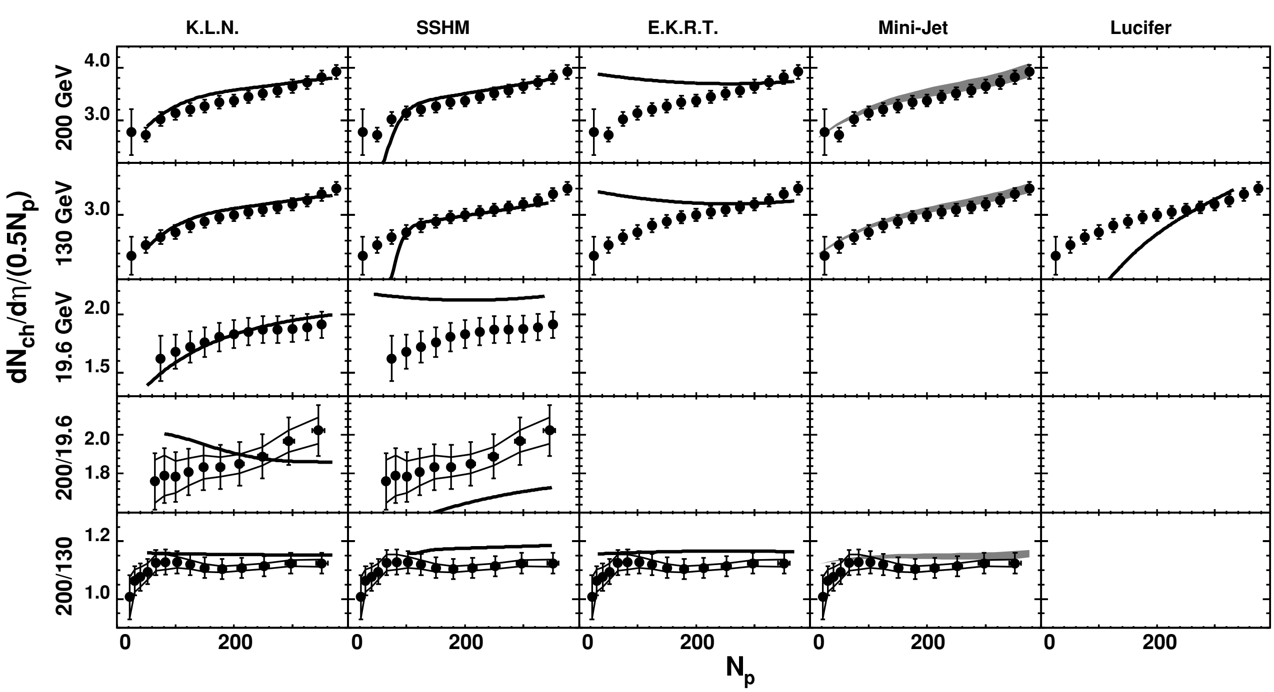

FIG. 16. $dN_{ch}/d\eta$ per pair of participants compared to theoretical models. KLN [49], SSHM [52], EKRT [48], Minijet [50] and LUCIFER [56]. The band shows the range of prediction for the Minijet model.

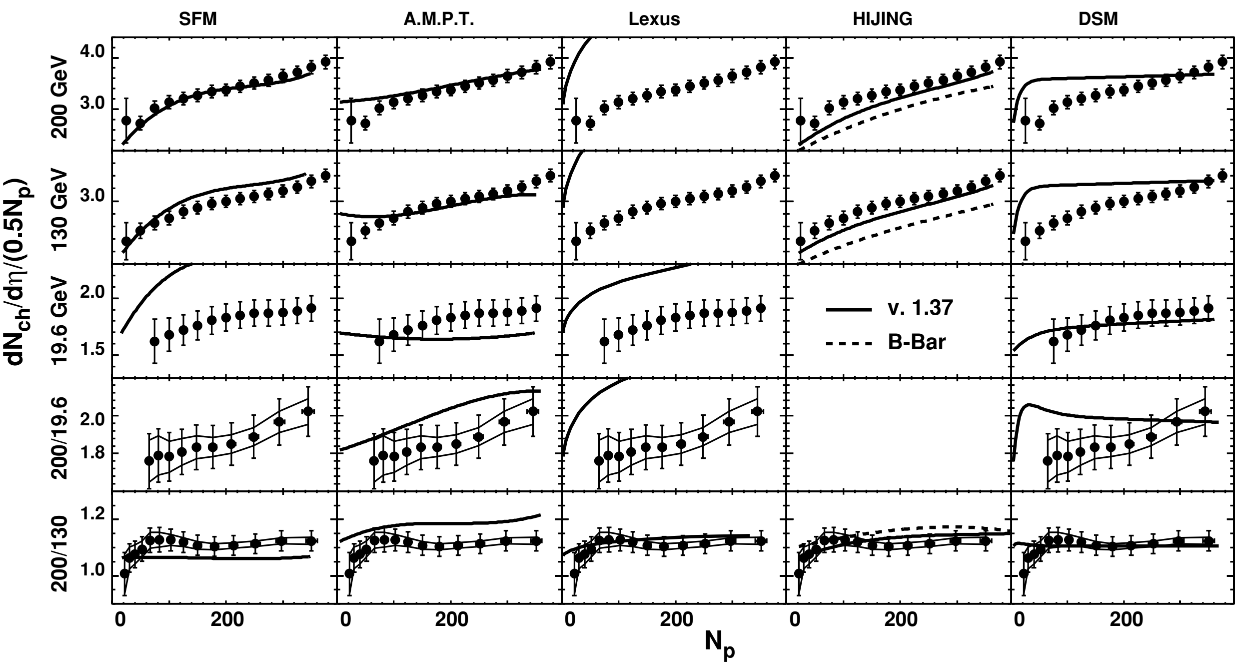

FIG. 17. Theoretical models compared to $dN_{\rm ch}/d\eta$ per pair of participants: SFM [55], AMPT [51], LEXUS [57], HIJING [15,46], and DSM [53].

between the existing theoretical models[7] and the data for 19.6, 130, and 200 GeV. Brief descriptions of the models and their main characteristics are given next.

One of the more commonly used Monte Carlo event generators is HIJING [15,46]. This model, like several others, uses pQCD for initial minijet production and the Lund string model [47] for jet fragmentation and hadronization. HIJING also includes jet quenching and nuclear shadowing. This type of model typically has two components, a soft part proportional to N_p and a hard part proportional to N_e, which partly motivated the discussion in Sec. IV D 2. There are also the so-called saturation models, which also rely on pQCD and predict that at some fixed scale the gluon and quark phase-space density saturates, thus limiting the number of produced quarks and gluons. An example of this type of model is EKRT [48], which is referred to as a final state saturation model. In this paper, comparisons are also made to another parton saturation type model, KLN [49], which is an initial state saturation model, and to models related to HIJING, namely, Minijet [50] and AMPT [51]. AMPT is a multiphase transport model and extends HIJING by including explicit interactions between initial minijet partons and final state hadronic interactions. Minijet follows the same two-component model as HIJING but also incorporates an energy-dependent cutoff scale, similar to the saturation models.

The other models are listed briefly below. SSHM and SFM do not have a designated short identifier, so they were named somewhat arbitrarily here, based on the physics the models incorporate. SSHM (saturation for semi-hard minijet) [52] is also a two-component model: it is pQCD-based for semihard partonic interactions, while for the soft particle production it uses the wounded nucleon model. DSM [53], the dual string model, is basically the dual parton model [54], with the inclusion of strings. SFM (string fusion model) [55] is a string model that includes hard collisions, collectivity in the initial state (string fusion), and rescattering of the produced secondaries. Finally, there are the hadronic models, LUCIFER [56], a cascade model with input fixed from lower energy data, and LEXUS [57], a linear extrapolation of ultrarelativistic nucleon-nucleon scattering data to nucleus-nucleus collisions.

The available model results range from predicting (or post-dicting) $dN_{\rm ch}/d\eta$ at one energy to predicting both $dN_{\rm ch}/d\eta$ and $dE_T/d\eta$ at 19.6, 130 and 200 GeV. The models have varying success in reproducing the data.

In Fig. 16, KLN is among the most successful at describing the $dN_{\rm ch}/d\eta$ centrality dependence for all three energies. However, at $\sqrt{s_{NN}} = 19.6$ GeV, the theoretical curve is steeper than the data. This results in a reversed centrality dependence relative to the data for the 200 to 19.6 GeV ratio. SSHM describes the 130 and 200 GeV data well, for centralities above $N_p \sim 100$, which is the approximate limit of applicability for this and other saturation models. For the less central events, the model values are lower than the data. At 19.6 GeV, the model values are significantly higher than the data. The saturation model EKRT describes the central points at both energies but overshoots the more peripheral data points and thus does not reproduce the general centrality dependence of the data. For the nonsaturation models included in this figure, Minijet reproduces both the overall scale and the centrality and energy dependence of the data rather well, while the cascade model

[7] Models are presented as the best fit by the polynomial of the lowest degree which is closer than 1% to any theoretical point provided by the authors of the models. The polynomial is plotted in the range where points are provided.

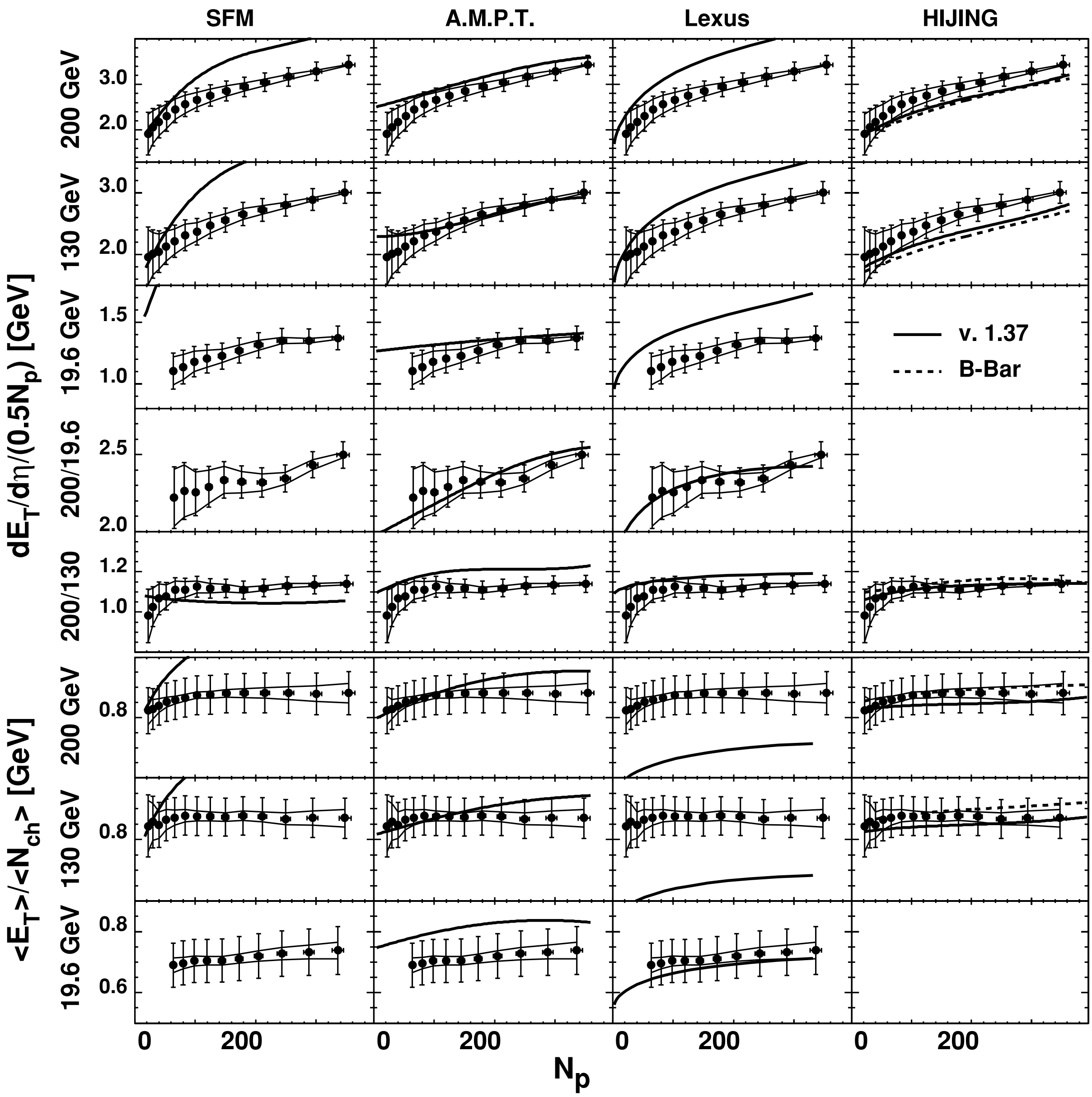

FIG. 18. Theoretical models compared to $dE_T/d\eta$ per pair of participants (upper panels) and per produced charged particle (lower panels): SFM [55], AMPT [51], LEXUS [57], and HIJING [15,46].

LUCIFER describes the central points at 130 GeV well but undershoots the less central values at this energy.

Most of the models included in Fig. 17 provided values for all three energies: 19.6, 130, and 200 GeV. SFM is in reasonable agreement with the 130 and 200 GeV data, but gives much larger values than the data at 19.6 GeV. AMPT is in overall good agreement with the data for the two higher energies, except for the increasing trend in $dN_{\rm ch}/d\eta$ at the most peripheral events, which is not seen in the experimental data. At the lower energy, the $N_{\rm ch}$ centrality behavior is underestimated. LEXUS rather severely overshoots the data for all energies, indicating that nucleus-nucleus effects are not accounted for. The HIJING models (version 1.37 and a new version with implemented baryon junctions, HIJING B-$\bar{\rm B}$) only provide points at 130 and 200 GeV and are in reasonable agreement with the data at those energies, but generally give somewhat lower values. The curves shown include quenching and shadowing implemented in HIJING. DSM describes 19.6 GeV reasonably well for all centralities and the more central bins for 130 and 200 GeV, but it overpredicts the values for semicentral and peripheral events.

Figure 18 shows the results for the models that provide data for both $dN_{\rm ch}/d\eta$ and $dE_T/d\eta$. For $dE_T/d\eta$, LEXUS and SFM consistently overshoot the data for all energies. In the ratio $E_T/N_{\rm ch}$, LEXUS gives values that are too low except at the lowest energy, 19.6 GeV. That might indicate that the hadronization mechanism allows too little energy per particle. The SFM gives values that are too large, except for the most peripheral bin, which suggests that the particles are assigned transverse masses that are too large. The HIJING versions and the related AMPT model are in reasonable agreement with the data for both $dE_T/d\eta$ and $E_T/N_{\rm ch}$.[8]

Also shown in Fig. 18 are the ratios of results at 200 to 19.6 GeV, and 200 to 130 GeV, for $dE_T/d\eta$. These results, especially the comparison of the 200 to 19.6 GeV data, are intended to make a more precise check of the $\sqrt{s_{NN}}$ dependence of the models. SFM fails to describe the 19.6 GeV data and thus cannot describe the energy dependence probed by these ratios, unlike LEXUS which, however, does not agree well with the individual data curves for 19.6, 130, and 200 GeV. AMPT and the HIJING versions reproduce the values of the ratios well, as expected since they are in reasonable agreement with the individual curves. AMPT and HIJING are also successful in describing the $E_T/N_{\rm ch}$ ratio, as illustrated in the lower panels of Fig. 18.

To summarize, most models reproduce at least some of the data fairly well, but most fail in describing all the data. Since the model results typically are given without systematic errors, it is not entirely straightforward to quantify the level of agreement or disagreement with the data. Qualitatively, the models that are most successful in describing both $dE_T/d\eta$ and $dN_{\rm ch}/d\eta$ in terms of the overall trends, regarding both centrality dependence and energy dependence, are AMPT and the HIJING versions. KLN and Minijet unfortunately do not give information on $dE_T/d\eta$ but are successful in describing the $dN_{\rm ch}/d\eta$ results. The $dN_{\rm ch}/d\eta$ results thus can either be described by the initial state saturation scenario (KLN) or by the minijet models that need an energy-dependent minijet cutoff scale as described in [46,50] to reproduce the data.

V. SUMMARY

This paper presents a systematic study of the energy and centrality dependence of the charged particle multiplicity and transverse energy at midrapidity at $\sqrt{s_{NN}} = 19.6$, 130, and 200 GeV.

The yields, divided by the number of participant nucleons, show a consistent centrality dependence (increase from peripheral to central) between $dE_T/d\eta$ and $dN_{\rm ch}/d\eta$ for all energies. Furthermore, the increase in the ratio $E_T/N_{\rm ch}$ from 19.6 to 200 GeV is consistent with a 20% increase in $\langle m_T\rangle$ with increasing $\sqrt{s_{NN}}$. The ratio $E_T/N_{\rm ch}$ shows only a weak centrality dependence at RHIC energies.

For the $\sqrt{s_{NN}}$ dependence, comparisons were made not only among RHIC results but also with data from lower energy fixed-target experiments at SPS, AGS, and Schwer-Ionen-Synchrotron (SIS). A phenomenological fit, scaling logarithmically with $\sqrt{s_{NN}}$, describes well both $dE_T/d\eta$ and $dN_{\rm ch}/d\eta$ for the most central collisions for all energies.

Using the fit results, one can delineate two regions with different particle production mechanisms. The region below SPS energy is characterized by a steep increase in $E_T/N_{\rm ch} \sim \langle m_T\rangle$ with $\sqrt{s_{NN}}$, whereas for the energies above SPS, $E_T/N_{\rm ch}$ is weakly dependent on $\sqrt{s_{NN}}$.

Within the systematic errors of the measurements, the shape of the centrality curves of $dN_{\rm ch}/d\eta/(0.5N_p)$ vs. N_p were found to be the same in the range of RHIC energies and to scale with $\ln(\sqrt{s_{NN}})$. The same must be true for E_T because $E_T/N_{\rm ch}$ has a very weak centrality dependence.

Based on the $dE_T/d\eta$ measurements, the Bjorken energy density estimates were performed and $\epsilon_{Bj}\cdot\tau$ was determined to be 5.4 ± 0.6 GeV fm$^{-2}\,c^{-1}$ at $\sqrt{s_{NN}} = 200$ GeV for the most central bin. This is in excess of what is believed to be sufficient for a phase transition to the new state of matter. The energy density increases by about a factor of 2.6 from the top SPS energy to the top RHIC energy.

Finally, a comparison between the RHIC $dN_{\rm ch}/d\eta$ and $dE_T/d\eta$ data and a collection of models was performed. A few models, notably HIJING and AMPT, reproduce both $dE_T/d\eta$ and $dN_{\rm ch}/d\eta$ rather well for several energies.

ACKNOWLEDGMENTS

We thank the staff of the Collider-Accelerator and Physics Departments at Brookhaven National Laboratory and the staff of the other PHENIX participating institutions for their vital contributions. We are grateful for information provided by the model authors. In particular, we thank A. Accardi, S. Barshay, S. Jeon, S. Kahana, D. Kharzeev, Z. Lin, N. Armesto Perez, R. Ugoccioni, V. T. Pop, and X. N. Wang for helpful correspondence. We acknowledge support from the U.S. Department of Energy, Office of Science, Nuclear Physics Division; the National Science Foundation, Abilene Christian University Research Council, Research Foundation of SUNY, and Dean of the College of Arts and Sciences, Vanderbilt University (USA); Ministry of Education, Culture, Sports, Science, and Technology and the Japan Society for the Promotion of Science (Japan); Conselho Nacional de Desenvolvimento Científico e Tecnológico and Fundação de Amparo à Pesquisa do Estado de São Paulo (Brazil); Natural Science Foundation of China (People's Republic of China); Centre National de la Recherche Scientifique, Commissariat à l'Énergie Atomique, and Institut National de Physique Nucléaire et de Physique des Particules (France); Bundesministerium für Bildung und Forschung, Deutscher Akademischer Austausch Dienst, and Alexander von Humboldt Stiftung (Germany); Hungarian National Science Fund, OTKA (Hungary); Department of Atomic Energy and Department of Science and Technology (India); Israel Science Foundation (Israel); Korea Research Foundation and Center for High Energy Physics (Korea); Russian Ministry of Industry, Science and Tekhnologies, Russian Academy of Science, Russian Ministry of Atomic Energy (Russia); VR and the Wallenberg Foundation (Sweden); the U.S. Civilian Research and Development Foundation for the Independent States of the Former Soviet Union; the US-Hungarian NSF-OTKA-MTA; the US-Israel Binational Science Foundation; and the 5th European Union TMR Marie-Curie Programme.

APPENDIX A: RECALCULATION OF THE NON-PHENIX EXPERIMENTAL DATA

Comparisons of $dE_T/d\eta$ and $dN_{\rm ch}/d\eta$ between different experiments can be made only if the results are presented

[8]Note that the HIJING versions available at the time the data were collected and used for predictions were in worse agreement with the data [10]. This was before energy loss and minijet separation/cutoff scale parameters were updated.

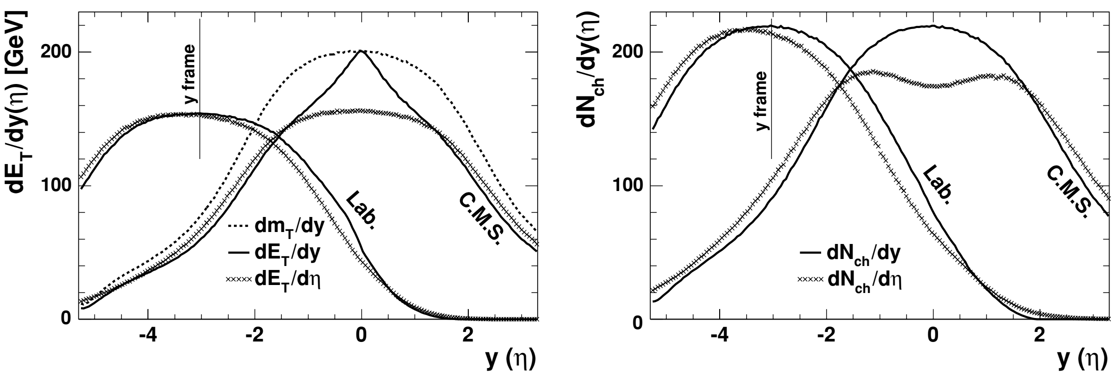

FIG. 19. Simulated E_T (left) and N_{ch} (right) distributions in rapidity and pseudorapidity units in c.m.s. and Lab. systems.

in the same coordinate system since these values are not boost invariants. In some cases a full set of identified particles measured by one experiment can be recalculated into E_T and N_{ch}. Each case that involves handling non-PHENIX published data is separately explained in this Appendix.

1. General

Figure 19 shows simulated rapidity distributions for E_T and N_{ch} in the c.m.s. and Lab. frames. Plots presented here are for illustrative purposes only. The invariant distributions which do not change their shape under transition from Lab. to c.m.s. are dm_T/dy and dN_{ch}/dy, while all others do.

In the c.m.s. system, the transition from η to y at midrapidity requires a scaling factor between 1.2 and 1.3. An accurate determination of this coefficient from the published data of other experiments is not always possible; therefore for the SPS and AGS energies a coefficient of 1.25 was used. Because of the definition of E_T used in this paper, $dE_T/dy \approx dm_T/dy$, around midrapidity, where m_T is a quadratic sum of the particle mass and transverse momentum: $m_T = \sqrt{m^2 + p_T^2}$.

In the Lab. system $dN_{\text{ch}}/dy \approx dN_{\text{ch}}/d\eta$ and $dE_T/dy \approx dE_T/d\eta$ at maximum rapidity. A 1.04 conversion factor was assigned to the transition from η to y in the Lab. system.

An error of 5% was assigned to any converted value. This error also absorbs uncertainties on various assumptions used in the calculations. For example, the contribution of neutral particles to the total E_T is assumed to be

$$\begin{aligned} E_T^{\pi^0} &= \left(E_T^{\pi^+} + E_T^{\pi^-}\right)/2, \\ E_T^{K^0} &= E_T^{K^+} + E_T^{K^-}, \\ E_T^{n} + E_T^{\bar{n}} &= E_T^{p} + E_T^{\bar{p}}. \end{aligned} \tag{A1}$$

2. Averaging procedure

Average values were calculated for $N_p = 25, 50, \ldots, 375$. The centrality bin corresponding to a given N_p can be different in different experiments. $dN_{\text{ch}}/d\eta$ per participant and the associated error were deduced by a weighted average interpolation from the two nearest values of each experiment. The closest value was required to be within a proximity of 25 participants from the N_p value. The error bars are multiplied by the S factor, where $S = \sqrt{\chi^2/\text{n.d.f.}}$ if $\chi^2/\text{n.d.f.} > 1$ or $S = 1$ otherwise. See the Particle Data Group reference [20] for details.

3. NA49

Table III lists the identified particle yields in the most central events at midrapidity at $\sqrt{s_{NN}} = 17.2$ GeV, as shown in Fig. 6 in Ref. [17]. The total yields per participant and number of participants in Table IV are taken from Fig. 10 in Ref. [17]. Using shapes of the dN/dy distributions shown in Fig. 7 of Ref. [17] for different centrality bins, the quantities tabulated in Tables III and IV can be converted into $dE_T/d\eta$ and $dN_{\text{ch}}/d\eta$ per participant pair at midrapidity. Systematic errors on particle yields are given in Table 1 in the same reference. The systematic errors for this value are not mentioned in the paper, therefore they were taken from [19]. The results used in this paper are also given in Table IV.

For the same and lower $\sqrt{s_{NN}}$, the identified particle yields and $\langle m_T \rangle$ were reconstructed using formula (1) and Fig. 1 in Ref. [18] and Table II and formulas (1) and (2) in Ref. [19]. The data obtained from the tables and the fits are summarized in Table V. Using dN/dy and $\langle m_T \rangle$, the values of $dE_T/d\eta$ and $dN_{\text{ch}}/d\eta$, were recalculated in the c.m.s. frame. The accuracy of the procedure was verified by the consistency of results presented in Tables V and VI.

The single E_T point in Fig. 13 is taken from [31] as 405 GeV and scaled up by 10%, then divided by pairs of $N_p = 390$ as explained in the text. This point does not agree with the value of E_T deduced from [17–19].

4. WA98

The centrality dependencies of E_T, N_{ch}, and E_T/N_{ch} were read from the plots in Figs. 7 and 14 in Ref. [25] and converted to the c.m.s. frame. Results are summarized in Table VII.

TABLE III. Results on identified particle yields in the most central events published by NA49 at midrapidity at $\sqrt{s_{NN}} = 17.2$ GeV taken from Fig. 6 in Ref. [17].

Particle	π^+	π^-	K^+	K^-	p	$\bar{p}$
dN/dy	167	165	32	15	33	5
Error	10	10	4	5	1.5	0.5

TABLE IV. Total yields of identified particles per participant and mean momentum at midrapidity in different centrality bins published by NA49 (P) at $\sqrt{s_{NN}} = 17.2$ GeV, from Figs. 8 and 10 in Ref. [17]. Recalculated values (R) are plotted in Figs. 11 and 12.

P	N_p	362	305	242	189	130	72	2
P	Error	10	15	15	15	10	5	
P	$\langle dN^{\pi}/dy/N_p \rangle$	1.65	1.64	1.55	1.48	1.40	1.42	1.42
P	Error	0.08	0.08	0.08	0.08	0.08	0.08	0.08
P	$\langle p_T^{\pi^+} \rangle$ (GeV/c)	0.29	0.31	0.30	0.30	0.30	0.29	0.28
P	$\langle p_T^{\pi^-} \rangle$ (GeV/c)	0.27	0.31	0.29	0.30	0.30	0.30	0.28
P	$dN^{K^+}/dy/N_p$	0.27	0.27	0.22	0.19	0.16	0.14	0.10
P	Error	0.02	0.02	0.02	0.02	0.02	0.02	0.02
P	$\langle p_T^{K^+} \rangle$ (GeV/c)	0.57	0.54	0.50	0.49	0.53	0.55	0.45
P	$dN^{K^-}/dy/N_p$	0.15	0.15	0.12	0.10	0.09	0.07	0.06
P	Error	0.01	0.01	0.01	0.01	0.01	0.01	0.01
P	$\langle p_T^{K^-} \rangle$ (GeV/c)	0.57	0.55	0.53	0.51	0.55	0.51	0.42
P	$\langle p_T^{p} \rangle$ (GeV/c)	0.77	0.74	0.75	0.73	0.70	0.65	0.54
P	$dN^{\bar{p}}/dy/N_p$	0.03	0.03	0.03	0.03	0.03	0.02	0.02
P	Error	0.005	0.005	0.005	0.005	0.005	0.005	0.005
P	$\langle p_T^{\bar{p}} \rangle$ (GeV/c)	0.87	0.84	0.80	0.75	0.78	0.70	0.48
R	$dE_T/d\eta/(0.5N_p)$ (GeV)	1.47	1.50	1.35	1.29	1.23	1.15	1.00
R	Error (GeV)	0.11	0.11	0.10	0.10	0.10	0.11	0.07
R	$dN_{\mathrm{ch}}/d\eta/(0.5N_p)$	1.75	1.74	1.62	1.54	1.46	1.44	1.38
R	Error	0.12	0.12	0.11	0.11	0.11	0.12	0.08

TABLE V. Temperatures of the identified particles published by NA49 at different $\sqrt{s_{NN}}$, as extracted from [18,19]. The yields are results of the fits of the parametrizations given in these publications.

				$\sqrt{s_{NN}} = 17.2$ GeV					
	π^+	π^-	K^+	K^-	p	$\bar{p}$	Λ	$\bar{\Lambda}$	d
T (GeV)	0.180	0.180	0.232	0.226	0.127	0.122	0.127	0.122	0.127
Error (GeV)	0.01	0.010	0.007	0.011	0.004	0.002	0.004	0.002	0.004
dN/dy	170.0	175.0	29.6	16.8	23.0	1.4	16.0	3.5	0.32
Error	9.0	9.0	1.5	0.8	7.4	0.23	6.1	0.67	0.23
				$\sqrt{s_{NN}} = 12.4$ GeV					
	π^+	π^-	K^+	K^-	p	$\bar{p}$	Λ	$\bar{\Lambda}$	d
T (GeV)	0.179	0.179	0.230	0.217	0.133	0.120	0.133	0.120	0.133
Error (GeV)	0.01	0.010	0.008	0.007	0.003	0.001	0.003	0.001	0.003
dN/dy	132.0	140.0	24.6	11.7	29.0	0.7	17.5	0.8	0.85
Error	7.0	7.0	1.2	0.6	6.2	0.06	4.4	0.08	0.28
				$\sqrt{s_{NN}} = 8.7$ GeV					
	π^+	π^-	K^+	K^-	p	$\bar{p}$	Λ	$\bar{\Lambda}$	d
T (GeV)	0.169	0.169	0.232	0.226	0.130	0.137	0.130	0.137	0.130
Error (GeV)	0.01	0.01	0.007	0.007	0.002	0.004	0.002	0.004	0.002
dN/dy	96.6	106.0	20.1	7.6	40.0	0.28	17.2	0.28	1.25
Error	6.0	6.0	1.0	0.4	5.8	0.08	2.9	0.08	0.37

TABLE VI. Recalculated NA49 results, as plotted in Figs. 13 and 14.

$\sqrt{s_{NN}}$ (GeV)	17.2	12.4	8.7
N_p	363 ± 10	352 ± 10	352 ± 10
$dE_T/d\eta/(0.5N_p)$ (GeV)	1.50 ± 0.11	1.16 ± 0.09	0.94 ± 0.07
$dN_{\mathrm{ch}}/d\eta/(0.5N_p)$	1.86 ± 0.08	1.54 ± 0.07	1.24 ± 0.06
E_T/N_{ch} (GeV)	0.81 ± 0.06	0.78 ± 0.06	0.76 ± 0.06

TABLE VII. Published (P) WA98 results at $\sqrt{s_{NN}} = 17.2$ GeV taken from Figs. 7 and 14 in Ref. [25], and recalculated (R) results plotted in Figs. 11–14. Additional systematic errors are shown in the plots.

P	N_p				382	357	311	269	234	201	174	148	128	109	91	75	62	49	39
P	Error				11	9	7	7	6	5	5	4	4	4	4	3	3	2	11
P	$dE_T/d\eta/(0.5N_p)$ (GeV)				2.09	2.06	2.06	2.05	2.03	2.00	1.95	1.96	1.93	1.87	1.84	1.78	1.73	1.70	1.59
P	Error (GeV)				0.12	0.12	0.12	0.12	0.12	0.12	0.11	0.11	0.11	0.11	0.12	0.14	0.15	0.17	0.18
R	$dE_T/d\eta/(0.5N_p)$ (GeV)				2.00	1.97	1.97	1.97	1.95	1.92	1.88	1.88	1.85	1.80	1.76	1.71	1.67	1.63	1.53
R	Error (GeV)				0.12	0.11	0.11	0.11	0.12	0.11	0.11	0.11	0.11	0.11	0.12	0.13	0.15	0.17	0.18
P	N_p	381	355	310	268	231	199	171	145	124	105	87	72	58	46	36	27	20	13	9
P	Error	10	9	8	7	6	6	6	5	5	5	4	5	4	3	3	3	2	2	12
P	$dN_{ch}/d\eta/(0.5N_p)$	2.66	2.64	2.62	2.60	2.58	2.54	2.50	2.49	2.43	2.40	2.34	2.32	2.31	2.29	2.20	2.17	2.13	2.17	2.22
P	Error	0.09	0.09	0.10	0.10	0.10	0.10	0.11	0.11	0.11	0.12	0.14	0.17	0.19	0.21	0.23	0.25	0.26	0.29	0.31
R	$dN_{ch}/d\eta/(0.5N_p)$	2.13	2.11	2.10	2.08	2.07	2.03	2.00	2.00	1.94	1.92	1.88	1.85	1.85	1.83	1.76	1.74	1.71	1.74	1.78
R	Error	0.07	0.08	0.08	0.08	0.08	0.08	0.09	0.09	0.09	0.10	0.12	0.14	0.16	0.16	0.18	0.20	0.21	0.23	0.25
P	N_p				383	359	315	276	242	211	185	160	140	123	106	91	78	66	56	49
P	Error				10	9	8	7	6	5	4	4	3	4	6	6	6	5	5	11
P	E_T/N_{ch} (GeV)				0.78	0.78	0.79	0.80	0.80	0.81	0.79	0.79	0.81	0.81	0.81	0.80	0.79	0.78	0.77	0.77
P	Error (GeV)				0.06	0.06	0.06	0.06	0.06	0.06	0.06	0.06	0.06	0.06	0.06	0.06	0.06	0.06	0.06	0.06
R	E_T/N_{ch} (GeV)				0.94	0.94	0.95	0.96	0.96	0.97	0.95	0.95	1.00	0.98	0.97	0.96	0.94	0.94	0.93	0.93
R	Error (GeV)				0.07	0.07	0.07	0.07	0.07	0.07	0.07	0.07	0.07	0.07	0.07	0.07	0.07	0.07	0.07	0.07

5. NA45

The NA45/CERES collaboration did not publish results for $dN_{ch}/d\eta$ as a function of centrality at $\sqrt{s_{NN}} = 17.2$ GeV. The data were taken from Fig. 6.5 in Ref. [58], and a 10% error was assigned based on the analysis procedure. The number of participants was taken from the corresponding cross-section bin reported by the NA50 results [42]. At the lower energy, the results were originally published in [59] and then N_p was subsequently corrected (see [41], for example). The results presented in Fig. 4 of Ref. [41] for charged hadrons h^- and $(h^+ - h^-)$ were added together to get $dh/d\eta$ and then converted to $dN_{ch}/d\eta$ in the c.m.s. frame. The published and recalculated results are summarized in Table VIII.

6. NA50

Results on N_p are taken from Tables 1 and 2 in Ref. [42] and on multiplicity from Figs. 2 and 4 tabulated in captions in Ref. [42]. The systematic errors are mentioned in the text. There is some discrepancy in the results of NA50 and NA45 as shown in Fig. 12. In this respect the comparison made in Table 3 of Ref. [42] is unclear. The results were converted to the c.m.s. frame. Recalculated values are given in Table IX.

7. E802/E917

The centrality dependence of π^+, K^+ yields and $\langle m_T \rangle$ were recalculated from Tables V and VI in Ref. [60]. Number of participants are taken from Table II in the same publication. The results are presented in Table X.

TABLE VIII. Published (P) NA45 results at $\sqrt{s_{NN}} = 17.2$ GeV taken from Fig. 6.5 in Ref. [58] and at $\sqrt{s_{NN}} = 8.7$ GeV from Fig. 4 in Ref. [41], and recalculated (R) results plotted in Figs. 11 and 12.

				$\sqrt{s_{NN}} = 17.2$ GeV				
P	Bin	0–2.3	2.3–5	5–8	8–12	12–18	18–23	23–35
P	$dN_{ch}/d\eta$	420	350	300	250	210	170	125
R	N_p	360	331	300	264	220	179	132
R	Error	10.	10	9	8	7	7	6
R	$dN_{ch}/d\eta/(0.5N_p)$	1.87	1.69	1.60	1.51	1.53	1.52	1.52
R	Error	0.19	0.18	0.17	0.16	0.16	0.16	0.17
				$\sqrt{s_{NN}} = 8.7$ GeV				
P	N_p	368	335	287	238	183	120	
P	h^-	129	113	94	78	58	38	
P	Error	15	14	12	11	9	9	
P	$h^+ - h^-$	52	46	39	30	22	15	
P	Error	12	8	8	7	6	6	
R	$dN_{ch}/d\eta/(0.5N_p)$	1.35	1.30	1.27	1.25	1.21	1.21	
R	Error	0.08	0.08	0.08	0.09	0.10	0.12	

TABLE IX. Recalculated NA50 results plotted in Figs. 11 and 12.

			$\sqrt{s_{NN}} = 17.2$ GeV			
N_p	354	294	246	205	173	129
Error	12	10	8	8	8	11
$dN_{ch}/d\eta/(0.5N_p)$	1.98	1.98	1.94	1.95	1.95	2.10
Error	0.16	0.16	0.16	0.16	0.16	0.17
			$\sqrt{s_{NN}} = 8.7$ GeV			
N_p	356	295	245	204	170	127
Error	12	10	8	8	8	11
$dN_{ch}/d\eta/(0.5N_p)$	0.95	0.90	0.90	0.89	0.90	0.92
Error	0.10	0.09	0.09	0.09	0.09	0.09

K^-/K^+ ratio was assigned a value of 0.17 for all centralities based on Tables II and III in Ref. [61]. This is consistent with results reported in Fig. 6 in Ref. [62] and Fig. 11 in [63]. The proton production reported in Table IV in Ref. [60] was compared to measurements reported in Fig. 2 in [64] and Fig. 10 in [63] for different centrality bins. The results are consistent. $\bar{p}/p$ ratio was assigned a value of 0.0003 based on Fig. 11 in Ref. [63]. A 25% enhancement in π^-/π^+ ratio for low m_T reported in [65] for the most central bin is not clearly seen in Fig. 11 in [63] for all centralities. Such an enhancement would contribute an additional 8–9% to the total particle and transverse energy production. This is less than the systematic error on the result and the recalculation error, and thus this effect is not considered. The resulting values shown in Table X were recalculated to midrapidity in the c.m.s. frame.

For the lower $\sqrt{s_{NN}}$ the information about particle yields and $\langle m_T \rangle$ was extracted for π^+ and K^+ from Tables II and I in Ref. [66], respectively; for K^- from Table I in [67]; and for p from Fig. 2 in [64]. The same assumptions as above were made to recalculate values plotted in Figs. 13 and 14. The numbers are given in Table XI.

8. Averaging procedure at $\sqrt{s_{NN}} = 8.7$ GeV

The averaging procedure is slightly different for this curve. First the average results of NA45 and NA50 are produced.

TABLE X. Centrality dependence of the identified particles measured by E802/E866/E917 collaborations. Number of participant pairs is published (P) in Table II in Ref. [60]. π^+ and K^+ values are obtained by extrapolation (E) from E802 measurement very close to midrapidity. Data were taken from Tables V and VI in Ref. [60]. Proton data are a compilation of the results taken from Table IV in [60] and Fig. 2 in [64]. Recalculated values (R) are plotted in Figs. 11 and 12.

P	N_p pairs	181	168	152	134	113	89.5	62.5	26.9
E	dN^{π^+}/dy	64.5	56.8	47.6	39.6	33.3	25.8	17.8	6.89
E	Error	3.13	2.55	2.75	1.75	1.68	1.37	0.89	0.28
E	$\langle m_T^{\pi^+} \rangle$ (GeV)	0.398	0.392	0.387	0.385	0.375	0.365	0.362	0.361
E	Error	0.013	0.013	0.014	0.012	0.041	0.011	0.010	0.011
E	dN^{K^+}/dy	10.6	9.28	8.12	6.17	4.91	3.73	2.22	0.74
E	Error	0.45	0.37	0.32	0.27	0.21	0.16	0.11	0.04
E	$\langle m_T^{K^+} \rangle$ (GeV)	0.809	0.787	0.774	0.785	0.770	0.740	0.743	0.685
E	Error	0.034	0.032	0.028	0.028	0.030	0.027	0.025	0.021
E	dN^p/dy	62.8	57.0	49.4	43.0	33.7	25.2	16.5	6.2
E	Error	1.7	1.5	1.4	1	1	1	1	1
E	$\langle m_T^p \rangle$ (GeV)	1.25	1.26	1.24	1.23	1.21	1.19	1.17	1.14
R	$dE_T/d\eta/(0.5N_p)$	0.608	0.580	0.527	0.492	0.460	0.426	0.396	0.335
R	Error (GeV)	0.146	0.138	0.125	0.116	0.111	0.103	0.098	0.131
R	$dN_{ch}/d\eta/(0.5N_p)$	0.903	0.865	0.812	0.773	0.751	0.725	0.699	0.621
R	Error	0.135	0.130	0.122	0.116	0.112	0.108	0.108	0.207
R	E_T/N_{ch} (GeV)	0.673	0.670	0.649	0.636	0.612	0.588	0.567	0.540
R	Error (GeV)	0.127	0.123	0.120	0.117	0.115	0.111	0.111	0.112

TABLE XI. Recalculated values from E802/E917 experiments plotted in Figs. 13 and 14.

$\sqrt{s_{NN}}$ (GeV)	4.84	4.27	3.81
$dE_T/d\eta/(0.5N_p)$ (GeV)	0.579 ± 0.087	0.498 ± 0.075	0.405 ± 0.061
$dN_{ch}/d\eta/(0.5N_p)$	0.851 ± 0.128	0.787 ± 0.118	0.678 ± 0.102
E_T/N_{ch} (GeV)	0.680 ± 0.068	0.634 ± 0.063	0.598 ± 0.060

TABLE XII. Particle yields measured by FOPI experiment at midrapidity extracted from Fig. 21 in Ref. [68].

Z	1	2	3	4	5–6
$dM/d(\cos\theta)$	43	12	2	0.5	0.25
Error	4.3	1.2	0.2	0.05	0.025

Then at $N_p = 350$, this result is combined with the NA49 measurement using the weighted error method. A scaling coefficient before and after NA49 averaging is calculated. The NA45/NA50 combined result is scaled by this factor for all values of N_p.

9. FOPI

The FOPI results for $N_{\rm ch}$ were calculated for 400 A MeV based on the data plotted in Fig. 21 of Ref. [68]. The points were read at the angle corresponding to the midrapidity angle ($\theta = 55^\circ$) and then converted to $dN_{\rm ch}/d\eta$ resulting in 39 ± 4 at $\sqrt{s_{NN}} = 2.053$ GeV.

The corresponding number of participants for a 42-mb event sample is 359 based on Fig. 8 in Ref. [69]. Data for 150 A MeV were compiled based on the comparison between Figs. 13 and 14 in [68] and the used definition of rapidity y, resulting in $dN_{\rm ch}/d\eta = 40 \pm 5$ at $\sqrt{s_{NN}} = 1.937$ GeV.

The estimate of the E_T production at 400 A MeV is made based on a comparison of the total yields of the particles with $Z = 1$ in [68] and yields of protons and deuterons published in [70]. That allowed us to determine the number of all pions at midrapidity to be 20.6 and the number of all hadrons with $Z = 1$ to be 15.2. Assuming that the particle temperatures are equal to $T = 40$ MeV (exact numbers are published in [69,70]), one can estimate that the contribution to E_T from pions is $m_\pi + 3/2T$ and from baryons is $3/2T$, according to the definition of E_T used in this paper. The resulting number of 5.0 GeV is a lower limit estimate because the contribution of heavier particles is not considered. A conservative error of 30% is assigned to this number.

10. PHOBOS measurement at $\sqrt{s_{NN}} = 56$ GeV

The PHOBOS experiment published $dN_{\rm ch}/d\eta = 408 \pm 12({\rm stat}) \pm 30({\rm syst})$ at $\sqrt{s_{NN}} = 56$ GeV measured for $N_p = 330 \pm 4({\rm stat})^{+10}_{-15}({\rm syst})$ in [35]. In the same paper, $dN_{\rm ch}/d\eta$ per participant between 130 and 56 GeV was measured to increase by $1.31 \pm 0.04({\rm stat}) \pm 0.05({\rm syst})$. That allows the use of the averaged value at $\sqrt{s_{NN}} = 130$ GeV consistent with the PHOBOS result published in [36] to recalculate $dN_{\rm ch}/d\eta$ at $\sqrt{s_{NN}} = 56$ GeV with smaller systematic error. This value is plotted in Fig. 13.

APPENDIX B: OUTPUT TABLES

TABLE XIII. Results of the measurements by PHENIX at $\sqrt{s_{NN}} = 200$ GeV. Errors have the same dimension as the preceding value. Results are plotted in Figs. 5, 7, and 8.

Bin (%)	0–5	5–10	10–15	15–20	20–25	25–30	30–35	35–40	40–45	45–50	50–55	55–60	60–65	65–70
N_p	353	300	254	215	181	151	125	103	83.3	66.7	52.5	40.2	30.2	22.0
Syst. error	10.0	9.0	8.1	7.3	6.6	6.0	5.5	5.1	4.7	4.3	4.1	3.8	3.6	3.4
$A_\perp$(fm^2)	140	125.0	112	100	90.8	82.2	73.9	66.8	60.0	54.3	49.3	45.1	40.9	37.5
Syst. error	11.0	10.0	9.1	8.2	7.4	6.8	6.2	5.7	5.2	4.8	4.6	4.5	4.5	4.9
$dE_T/d\eta$ (GeV)	606	493	402	328	266	216	173	137	107	81.8	60.4	43.9	31.1	21.1
Stat. error	0.6	0.6	0.5	0.5	0.4	0.4	0.3	0.3	0.2	0.2	0.2	0.1	0.1	0.1
Bending syst. error	2.4	5.1	7.0	7.6	8.2	8.5	8.2	8.1	7.6	6.9	6.4	5.5	4.6	3.9
Full syst. error	32.0	27.0	22.0	19.0	16.0	14.0	12.0	11.0	9.5	8.1	7.2	5.9	4.9	4.0
$\varepsilon_{Bj}\tau$ (GeV fm^{-2} c^{-1})	5.4	4.9	4.5	4.1	3.7	3.3	2.9	2.6	2.2	1.9	1.5	1.2	1.0	0.7
Full syst. error	0.6	0.5	0.5	0.5	0.4	0.4	0.4	0.3	0.3	0.3	0.2	0.2	0.2	0.2
$dE_T/d\eta/(0.5N_p)$ (GeV)	3.43	3.28	3.16	3.05	2.94	2.86	2.76	2.66	2.57	2.45	2.30	2.18	2.06	1.92
Bending syst. error	0.01	0.03	0.05	0.07	0.09	0.12	0.14	0.17	0.19	0.22	0.27	0.31	0.36	0.43
Full syst. error	0.21	0.20	0.20	0.20	0.21	0.22	0.23	0.25	0.27	0.29	0.33	0.36	0.41	0.47
$dN_{\rm ch}/d\eta$	687	560	457	372	302	246	197	156	124	95.3	70.9	52.2	37.5	25.6
Stat. error	0.7	0.6	0.5	0.5	0.4	0.4	0.3	0.3	0.2	0.2	0.2	0.1	0.1	0.1
Bending syst. error	25.0	17.0	14.0	11.0	10.0	9.9	9.4	9.0	8.2	7.8	7.1	6.1	5.2	4.4
Full syst. error	37.0	28.0	22.0	18.0	16.0	14.0	12.0	11.0	9.6	8.6	7.6	6.5	5.4	4.5
$dN_{\rm ch}/d\eta/(0.5N_p)$	3.89	3.73	3.59	3.45	3.34	3.25	3.15	3.05	2.96	2.86	2.70	2.60	2.48	2.33
Bending syst. error	0.14	0.12	0.11	0.10	0.12	0.14	0.16	0.19	0.21	0.25	0.30	0.35	0.41	0.49
Full syst. error	0.23	0.22	0.21	0.21	0.21	0.22	0.24	0.26	0.28	0.32	0.36	0.41	0.46	0.55
$E_T/N_{\rm ch}$ (GeV)	0.881	0.879	0.881	0.882	0.881	0.880	0.875	0.874	0.866	0.858	0.851	0.840	0.828	0.823
Bending syst. error	0.032	0.026	0.021	0.017	0.015	0.012	0.011	0.010	0.011	0.013	0.017	0.023	0.032	0.047
Full syst. error	0.071	0.069	0.067	0.066	0.065	0.065	0.064	0.064	0.064	0.064	0.064	0.065	0.068	0.076

TABLE XIV. Results of the measurements by PHENIX at $\sqrt{s_{NN}} = 130$ GeV. Errors have the same dimension as the preceding value. Results are plotted in Figs. 5, 7, and 8.

Bin (%)	0–5	5–10	10–15	15–20	20–25	25–30	30–35	35–40	40–45	45–50	50–55	55–60	60–65	65–70
N_p	348	294	250	211	179	150	125	103	83.2	66.3	52.1	40.1	30.1	21.9
Syst. error	10.0	8.9	8.0	7.2	6.6	6.0	5.5	5.1	4.7	4.3	4.0	3.8	3.6	3.4
$A_\perp$(fm^2)	138	123	110	99.5	89.4	80.6	72.8	65.8	59.5	54.3	49.0	44.8	40.9	37.4
Syst. error	11.0	9.9	8.9	8.1	7.3	6.6	6.1	5.6	5.2	4.8	4.6	4.5	4.6	4.8
$dE_T/d\eta$ (GeV)	523	425	349	287	237	191	154	122	96.0	73.3	55.5	41.0	30.2	21.4
Stat. error	0.9	0.9	0.8	0.7	0.6	0.6	0.5	0.4	0.4	0.3	0.3	0.2	0.2	0.2
Bending syst. error	2.6	4.2	5.6	7.0	7.5	7.6	7.5	7.0	7.3	6.2	5.8	5.1	4.4	4.1
Full syst. error	27.0	22.0	19.0	16.0	14.0	12.0	11.0	9.4	8.8	7.3	6.5	5.5	4.7	4.2
$\varepsilon_{Bj}\tau$ (GeV fm^{-2} c^{-1})	4.7	4.3	3.9	3.6	3.3	3.0	2.6	2.3	2.0	1.7	1.4	1.1	0.9	0.7
Full syst. error	0.5	0.5	0.4	0.4	0.4	0.3	0.3	0.3	0.3	0.2	0.2	0.2	0.2	0.2
$dE_T/d\eta/(0.5N_p)$ (GeV)	3.01	2.89	2.80	2.72	2.65	2.56	2.47	2.37	2.31	2.21	2.13	2.05	2.01	1.95
Bending syst. error	0.01	0.03	0.05	0.07	0.09	0.10	0.12	0.14	0.19	0.20	0.24	0.29	0.34	0.45
Full syst. error	0.18	0.18	0.18	0.18	0.19	0.20	0.21	0.22	0.25	0.26	0.30	0.34	0.39	0.49
$dN_{\mathrm{ch}}/d\eta$	602	488	403	329	270	219	176	139	109	84.1	64.3	48.4	35.2	25.3
Stat. error	1.4	1.2	1.1	0.9	0.8	0.7	0.6	0.5	0.4	0.3	0.3	0.3	0.2	0.2
Bending syst. error	19.0	13.0	10.0	9.9	8.6	8.4	8.3	7.7	7.5	6.4	5.9	5.2	4.3	4.1
Full syst. error	28.0	22.0	17.0	15.0	13.0	11.0	10.0	9.1	8.4	7.0	6.3	5.4	4.5	4.1
$dN_{\mathrm{ch}}/d\eta/(0.5N_p)$	3.46	3.32	3.23	3.12	3.03	2.93	2.82	2.70	2.63	2.54	2.47	2.41	2.34	2.31
Bending syst. error	0.11	0.09	0.08	0.09	0.10	0.12	0.14	0.16	0.19	0.21	0.25	0.30	0.35	0.47
Full syst. error	0.19	0.18	0.17	0.18	0.18	0.19	0.21	0.22	0.25	0.27	0.31	0.35	0.41	0.52
E_T/N_{ch} (GeV)	0.869	0.870	0.867	0.874	0.877	0.873	0.875	0.876	0.878	0.871	0.864	0.847	0.857	0.844
Bending syst. error	0.028	0.023	0.019	0.016	0.015	0.014	0.014	0.016	0.020	0.025	0.033	0.043	0.060	0.083
Full syst. error	0.066	0.064	0.063	0.062	0.062	0.062	0.062	0.063	0.064	0.065	0.068	0.073	0.084	0.101

TABLE XV. Results of the measurements by PHENIX at $\sqrt{s_{NN}} = 19.6$ GeV. Errors have the same dimension as the preceding value. Results are plotted in Figs. 5, 7, and 8.

Bin (%)	0–5	5–10	10–15	15–20	20–25	25–30	30–35	35–40	40–45	45–50
N_p	336	288	243	204	172	144	120	98.4	79.8	63.8
Syst. error	9.7	8.8	7.9	7.1	6.4	5.9	5.4	5.0	4.6	4.3
$A_\perp$(fm^2)	133.0	119	106	95.6	85.8	77.2	69.7	62.7	56.7	51.3
Syst. error	11.0	9.6	8.6	7.8	7.0	6.4	5.8	5.3	4.9	4.6
$dE_T/d\eta$ (GeV)	230	194	164	134	109	88.4	72.0	58.1	45.3	35.2
Stat. error	0.8	0.8	0.8	0.7	0.5	0.5	0.4	0.4	0.3	0.3
Bending syst. error	1.7	2.6	2.9	4.0	3.8	3.8	3.9	3.9	3.9	3.4
Full syst. error	14.	12.	11.	9.3	7.8	6.7	6.0	5.3	4.8	4.0
$\varepsilon_{Bj}\tau$ (GeV fm^{-2} c^{-1})	2.2	2.0	1.9	1.8	1.6	1.4	1.3	1.2	1.0	0.9
Full syst. error	0.2	0.2	0.2	0.2	0.2	0.2	0.2	0.2	0.1	0.1
$dE_T/d\eta/(0.5N_p)$ (GeV)	1.37	1.35	1.35	1.31	1.27	1.22	1.20	1.18	1.13	1.10
Bending syst. error	0.01	0.02	0.02	0.04	0.05	0.05	0.07	0.08	0.10	0.11
Full syst. error	0.09	0.09	0.10	0.10	0.10	0.10	0.11	0.12	0.14	0.15
$dN_{\mathrm{ch}}/d\eta$	312	265	226	187	154	125	102	82.6	65.0	51.1
Stat. error	0.9	0.9	0.9	0.8	0.7	0.6	0.5	0.4	0.4	0.3
Bending syst. error	5.3	4.5	4.4	5.4	4.9	5.3	5.2	5.1	5.1	4.2
Full syst. error	21.0	18.0	15.0	13.0	11.0	9.7	8.5	7.4	6.6	5.4
$dN_{\mathrm{ch}}/d\eta/(0.5N_p)$	1.86	1.84	1.85	1.83	1.78	1.74	1.71	1.68	1.63	1.60
Bending syst. error	0.03	0.03	0.04	0.05	0.06	0.08	0.09	0.11	0.14	0.14
Full syst. error	0.14	0.14	0.14	0.14	0.14	0.15	0.16	0.17	0.19	0.20

TABLE XV. (*Continued.*)

Bin (%)	0–5	5–10	10–15	15–20	20–25	25–30	30–35	35–40	40–45	45–50
E_T/N_{ch} (GeV)	0.738	0.733	0.728	0.720	0.711	0.705	0.704	0.704	0.697	0.690
Bending syst. error	0.027	0.023	0.020	0.017	0.015	0.014	0.014	0.016	0.019	0.024
Full syst. error	0.078	0.076	0.075	0.073	0.072	0.071	0.071	0.071	0.072	0.072

TABLE XVI. Ratios of measured quantities at 200/130 and 200/19.6 GeV. The number of N_p is the average between two energies. The data are plotted in Fig. 6.

Bin (%)	0–5	5–10	10–15	15–20	20–25	25–30	30–35	35–40	40–45	45–50	50–55	55–60	60–65	65–70
							200/130 GeV							
N_p	350	297	252	213	180	150	125	103	83.2	66.5	52.3	40.2	30.2	22.0
Syst. error	10.0	9.0	8.1	7.3	6.6	6.0	5.5	5.1	4.7	4.3	4.1	3.8	3.6	3.4
$dE_T/d\eta/(0.5N_p)$	1.14	1.13	1.13	1.12	1.11	1.12	1.12	1.12	1.11	1.11	1.08	1.07	1.03	0.98
Bending syst. error	0.01	0.01	0.01	0.01	0.01	0.02	0.02	0.03	0.04	0.05	0.05	0.07	0.09	0.13
Full syst. error	0.04	0.04	0.04	0.04	0.04	0.05	0.05	0.05	0.06	0.06	0.07	0.08	0.10	0.13
$dN_{ch}/d\eta/(0.5N_p)$	1.12	1.12	1.11	1.11	1.10	1.11	1.12	1.13	1.13	1.13	1.10	1.08	1.06	1.01
Bending syst. error	0.01	0.01	0.01	0.01	0.01	0.01	0.02	0.02	0.03	0.03	0.03	0.03	0.04	0.07
Full syst. error	0.04	0.04	0.04	0.04	0.04	0.04	0.04	0.04	0.04	0.04	0.04	0.05	0.05	0.08
							200/19.6 GeV							
N_p	344	294	249	210	177	148	122	101	81.6	65.2				
Syst. error	10.0	9.0	8.1	7.3	6.6	6.0	5.5	5.1	4.7	4.3				
$dE_T/d\eta/(0.5N_p)$	2.50	2.43	2.34	2.32	2.32	2.34	2.29	2.25	2.26	2.22				
Bending syst. error	0.02	0.03	0.04	0.06	0.07	0.09	0.11	0.13	0.17	0.19				
Full syst. error	0.09	0.09	0.09	0.10	0.10	0.12	0.13	0.15	0.19	0.20				
$dN_{ch}/d\eta/(0.5N_p)$	2.09	2.03	1.94	1.89	1.87	1.87	1.84	1.81	1.82	1.79				
Bending syst. error	0.08	0.06	0.06	0.06	0.06	0.07	0.08	0.10	0.12	0.13				
Full syst. error	0.15	0.14	0.13	0.13	0.13	0.14	0.14	0.15	0.17	0.17				

TABLE XVII. Average values of $dN_{ch}/d\eta\,/(0.5N_p)$ at different $\sqrt{S_{NN}}$. An additional 5% error should be added to rows 17.2–4.8 GeV for the uncertainty related to recalculation to the center-of-mass system. The results are presented in Figs. 9 and 12.

N_p	375	350	325	300	275	250	225	200	175	150	125	100	75	50	25
$\sqrt{S_{NN}}$															
200 GeV	3.92	3.81	3.72	3.65	3.56	3.51	3.45	3.38	3.34	3.27	3.20	3.14	3.03	2.73	2.78
Error	0.13	0.13	0.12	0.12	0.12	0.12	0.12	0.11	0.12	0.12	0.12	0.13	0.13	0.13	0.43
130 GeV	3.41	3.31	3.22	3.16	3.11	3.07	3.04	3.00	2.96	2.89	2.83	2.73	2.65	2.53	2.36
Error	0.10	0.10	0.10	0.10	0.09	0.09	0.10	0.09	0.10	0.10	0.10	0.11	0.11	0.12	0.30
19.6 GeV		1.91	1.89	1.88	1.87	1.87	1.85	1.83	1.81	1.76	1.72	1.68	1.62		
Error		0.11	0.11	0.11	0.11	0.12	0.12	0.12	0.12	0.13	0.14	0.15	0.19		
17.2 GeV	1.97	1.93	1.90	1.88	1.83	1.80	1.78	1.75	1.72	1.69	1.66	1.66	1.61	1.54	1.45
Error	0.12	0.12	0.14	0.15	0.16	0.17	0.17	0.17	0.17	0.17	0.16	0.23	0.21	0.19	0.13
8.7 GeV	1.26	1.22	1.20	1.18	1.17	1.16	1.16	1.14	1.14	1.14	1.14	1.14			
Error	0.11	0.11	0.11	0.10	0.10	0.10	0.10	0.10	0.09	0.09	0.09	0.09			
4.8 GeV	0.92	0.89	0.85	0.81	0.78	0.76	0.75	0.74	0.72	0.71	0.70	0.67	0.64	0.63	
Error	0.14	0.13	0.13	0.12	0.12	0.11	0.11	0.11	0.11	0.11	0.11	0.14	0.18	0.21	

[1] H. Hahn *et al.*, Nucl. Instrum. Methods A **499**, 245 (2003).
[2] PHENIX Collaboration, K. Adcox *et al.*, Nucl. Instrum. Methods A **499**, 469 (2003).
[3] K. Adcox *et al.*, Nucl. Instrum. Methods A **497**, 263 (2003).
[4] L. Aphechetche *et al.*, Nucl. Instrum. Methods A **499**, 521 (2003).
[5] M. Allen *et al.*, Nucl. Instrum. Methods A **499**, 549 (2003).
[6] S. Adler *et al.*, Nucl. Instrum. Methods A **470**, 488 (2001).
[7] PHENIX Collaboration, K. Adcox *et al.*, Phys. Rev. Lett. **87**, 052301 (2001).
[8] PHENIX Collaboration, K. Adcox *et al.*, Phys. Rev. Lett. **86**, 3500 (2001).
[9] A. Milov for the PHENIX Collaboration, Nucl. Phys. **A698**, 171 (2002).
[10] A. Bazilevsky for the PHENIX Collaboration, Nucl. Phys. **A715**, 486 (2003).
[11] D. Silvermyr, Ph.D. thesis, Lund University, 2001.
[12] A. Milov, Ph.D. Thesis, Weizmann Institute of Science, 2002.
[13] PHENIX Collaboration, K. Adcox *et al.*, Phys. Rev. Lett. **88**, 242301 (2002).
[14] GEANT 3.2.1, CERN program library.
[15] X. N. Wang and M. Gyulassy, Phys. Rev. D **44**, 3501 (1991).
[16] PHENIX Collaboration, S. S. Adler *et al.*, Phys. Rev. C **69**, 034909 (2004).
[17] J. Bächler for the NA49 Collaboration, Nucl. Phys. **A661**, 45 (1999).
[18] M. van Leeuwen for the NA49 Collaboration, Nucl. Phys. **A715**, 161 (2003).
[19] NA49 Collaboration, S. V. Afanasiev *et al.*, Phys. Rev. C **66**, 054902 (2002).
[20] K. Hagiwara *et al.*, http://pdg.lbl.gov; Phys. Rev. D **66**, 010001 (2002).
[21] B. Hahn, D. G. Ravenhall, and R. Hofstadter, Phys. Rev. **101**, 1131 (1956); C. W. De Jager *et al.*, At. Data Nucl. Data Tables **24**, 479 (1974).
[22] PHOBOS Collaboration, B. B. Back *et al.*, Phys. Rev. Lett. **91**, 052303 (2003).
[23] E-802 Collaboration, T. Abbott *et al.*, Phys. Rev. C **63**, 064602 (2001).
[24] PHENIX Collaboration, K. Adcox *et al.*, Phys. Rev. C **66**, 024901 (2002).
[25] WA98 Collaboration, M. M. Aggarval *et al.*, Eur. Phys. J. C **18**, 651 (2001).
[26] PHENIX Collaboration, S. S. Adler *et al.*, Phys. Rev. Lett. **91**, 241803 (2003).
[27] PHOBOS Collaboration, B. B. Back *et al.*, nucl-ex/0301017.
[28] M. Gyulassy, Lec. Note Phys. **583**, 37 (2002).
[29] A. Krasnitz, Y. Nara, and R. Venugopalan, hep-ph/0305112; Nucl. Phys. **A727**, 427 (2003).
[30] J. D. Bjorken, Phys. Rev. D **27**, 140 (1983).
[31] NA49 Collaboration, T. Alber *et al.*, Phys. Rev. Lett. **75**, 3814 (1995).
[32] STAR Collaboration, J. Adams *et al.*, nucl-ex/0311017.
[33] BRAHMS Collaboration, I. G. Bearden *et al.*, Phys. Lett. **B523**, 227 (2001).
[34] BRAHMS Collaboration, I. G. Bearden *et al.*, Phys. Rev. Lett. **88**, 202301 (2002).
[35] PHOBOS Collaboration, B. B. Back *et al.*, Phys. Rev. Lett. **85**, 3100 (2000).
[36] PHOBOS Collaboration, B. B. Back *et al.*, Phys. Rev. C **65**, 061901 (2002).
[37] M. D. Baker *et al.* for the PHOBOS Collaboration, Nucl. Phys. **A715**, 65c (2003).
[38] T. S. Ullrich for the STAR Collaboration, Heavy Ion Phys. **21**, 143 (2004).
[39] T. S. Ullrich for the STAR Collaboration, Nucl. Phys. **A715**, 399 (2003).
[40] STAR Collaboration, J. Adams *et al.*, Phys. Rev. C **70**, 054907 (2004).
[41] CERES Collaboration, D. Mis̀kowiec, in *Proceedings of the 30th International Workshop on Gross Properties of Nuclei and Nuclear Excitations: Ultrarelativistic heavy-ion collisions, Hirschegg, Austria, January 13–19, 2002*, edited by M. Buballa, W. Nörenberg, B.-J. Schaefer, J. Wambach [Technical University of Darmstadt and Gesellschaft fürSchwerionenforschung (GSI), Darmstadt, 2002], p. 238–247, http://theory.gsi.de/hirschegg/2002/Proceedings/
[42] NA50 Collaboration, M. C. Abreu *et al.*, Phys. Lett. **B530**, 43 (2002).
[43] NA57 Collaboration, F. Antinori *et al.*, hep-ex/0406004.
[44] UA5 Collaboration, G. J. Alner *et al.*, Z. Phys. C **33**, 1 (1986).
[45] W. Thome *et al.*, Nucl. Phys. **B129**, 365 (1977).
[46] V. Topor Pop, M. Gyulassy, J. Barrette, C. Gale, X. N. Wang, N. Xu, and K. Filimonov, Phys. Rev. C **68**, 054902 (2003).
[47] B. Andersson *et al.*, Nucl. Phys. **B281**, 289 (2003).
[48] K. J. Eskola *et al.*, Nucl. Phys. **B570**, 379 (2000); Phys. Lett. **B497**, 39 (2001).
[49] D. Kharzeev and M. Nardi, Phys. Lett. **B507**, 121 (2001); D. Kharzeev and E. Levin, *ibid.* **B523**, 79 (2001).
[50] S. Lee and X. N. Wang, Phys. Lett. **B527**, 85 (2002).
[51] Z. W. Lin, S. Pal, C. M. Ko, B. A. Li, and B. Zhang, Phys. Rev. C **64**, 011902(R) (2001).
[52] A. Accardi, Phys. Rev. C **64**, 064905 (2001).
[53] R. Ugoccioni, Phys. Lett. **B491**, 253 (2000).
[54] A. Capella *et al.*, Phys. Rep. **236**, 225 (1994).
[55] N. Armesto Perez *et al.*, Phys. Lett. **B527**, 92 (2002); Eur. Phys. J. C **22**, 149 (2001).
[56] D. E. Kahana and S. H. Kahana, nucl-th/0208063.
[57] S. Jeon and J. Kapusta, Phys. Rev. C **63**, 011901(R) (2001).
[58] F. Ceretto, Ph.D. thesis, University of Heidelberg, 1998.
[59] H. Appelshäuser for the CERES Collaboration, Nucl. Phys. **A698**, 253 (2002).
[60] E802 Collaboration, L. Ahle *et al.*, Phys. Rev. C **59**, 2173 (1999).
[61] E802 Collaboration, L. Ahle *et al.*, Phys. Rev. C **58**, 3523 (1998).
[62] C. A. Ogilvie for the E866 and E917 Collaborations, Nucl. Phys. **A638**, 57c (1998).
[63] Y. Akiba for the E802 Collaboration, Nucl. Phys. **A610**, 139 (1996).
[64] E917 Collaboration, B. B. Back *et al.*, Phys. Rev. Lett. **86**, 1970 (2001).
[65] E802 Collaboration, L. Ahle *et al.*, Phys. Rev. C **57**, 466(R) (1998).
[66] E802 Collaboration, L. Ahle *et al.*, Phys. Lett. **B476**, 1 (2000).
[67] E802 Collaboration, L. Ahle *et al.*, Phys. Lett. **B490**, 53 (2000).
[68] FOPI Collaboration, W. Reisdorf *et al.*, Nucl. Phys. **A612**, 493 (1997).
[69] FOPI Collaboration, D. Pelte *et al.*, Z. Phys. A **357**, 215 (1997).
[70] FOPI Collaboration, B. Hong *et al.*, Phys. Rev. C **66**, 034901 (2002).